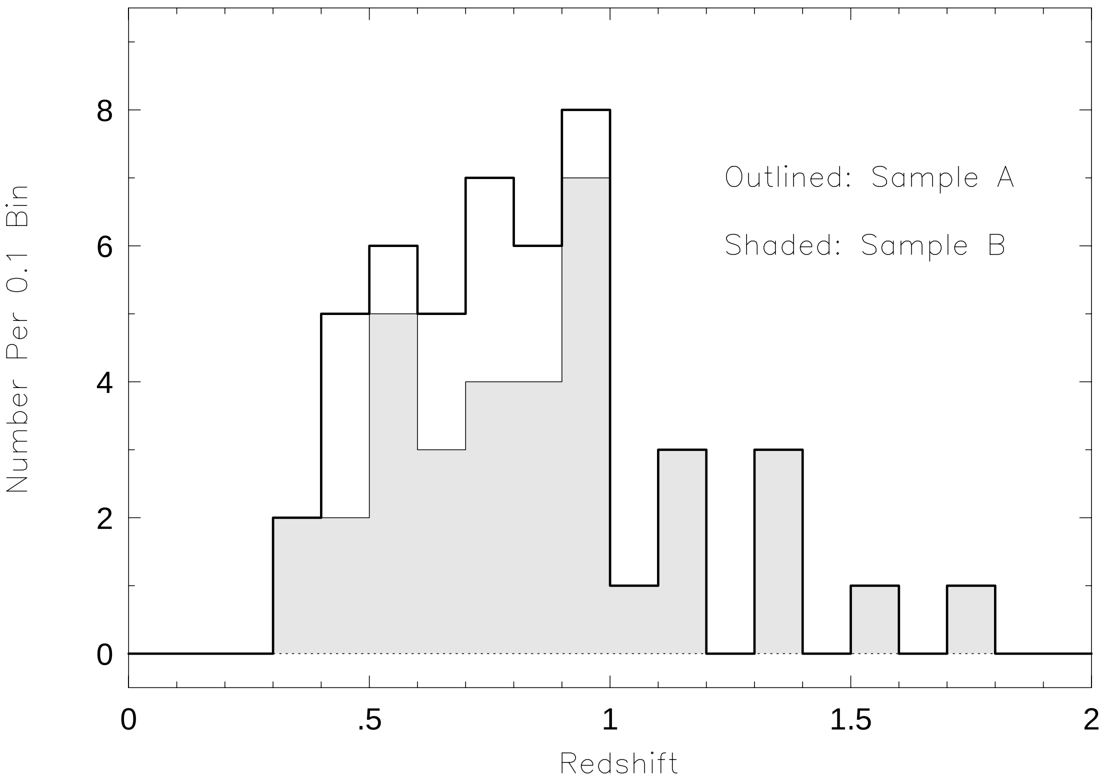

Fig. 3.1.— The number of observed systems per $\Delta z = 0.1$ redshift bin. The thick line histogram shows the full sample presented in Table 3.1, and the shaded region gives the distribution of Sample B. The highest redshifts are under represented and suffer a selection bias toward large equivalent widths.

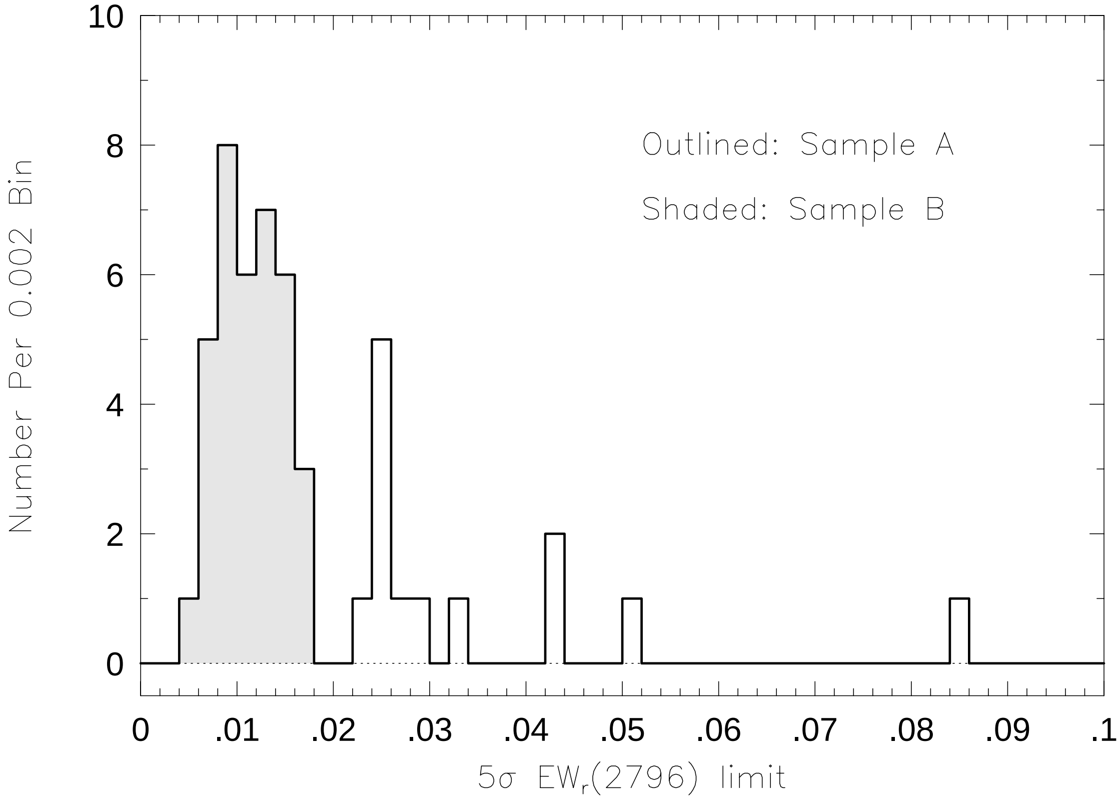

Fig. 3.2.— The number of systems per $\Delta \mathrm{EW_r} = 0.002$ equivalent width bin. Based upon simulations (see Chapter 4), and the natural gap in the distribution, a cutoff at a 5σ detection level 0.02 Å was chosen.

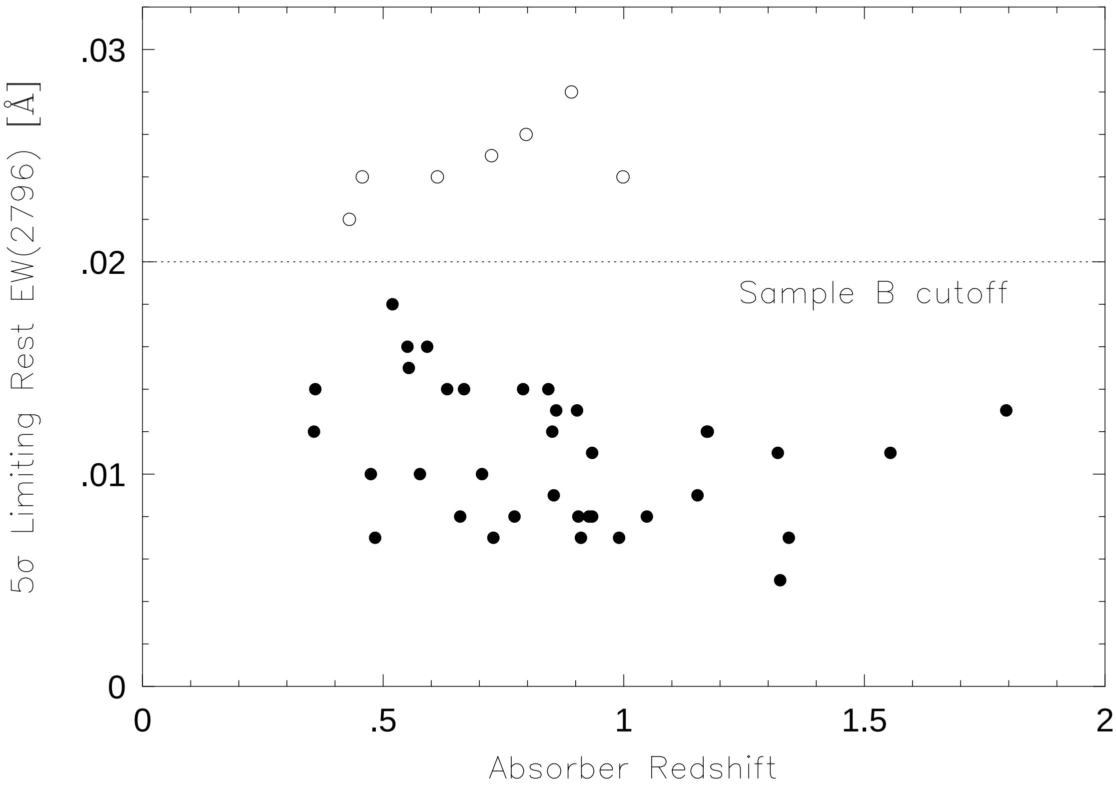

Fig. 3.3.— The rest–frame equivalent width detection limit (5σ) verses absorber redshift. The detection level of Sample B is fairly uniform with redshift; a Spearman–Kendall non–parametric test did suggest a weak anti–correlation, but it is negligible (see text and Table 3.4). A correlation in the limiting equivalent width is undesirable because it holds the potential of introducing a bias into the analysis of redshift evolution in the absorption profiles.

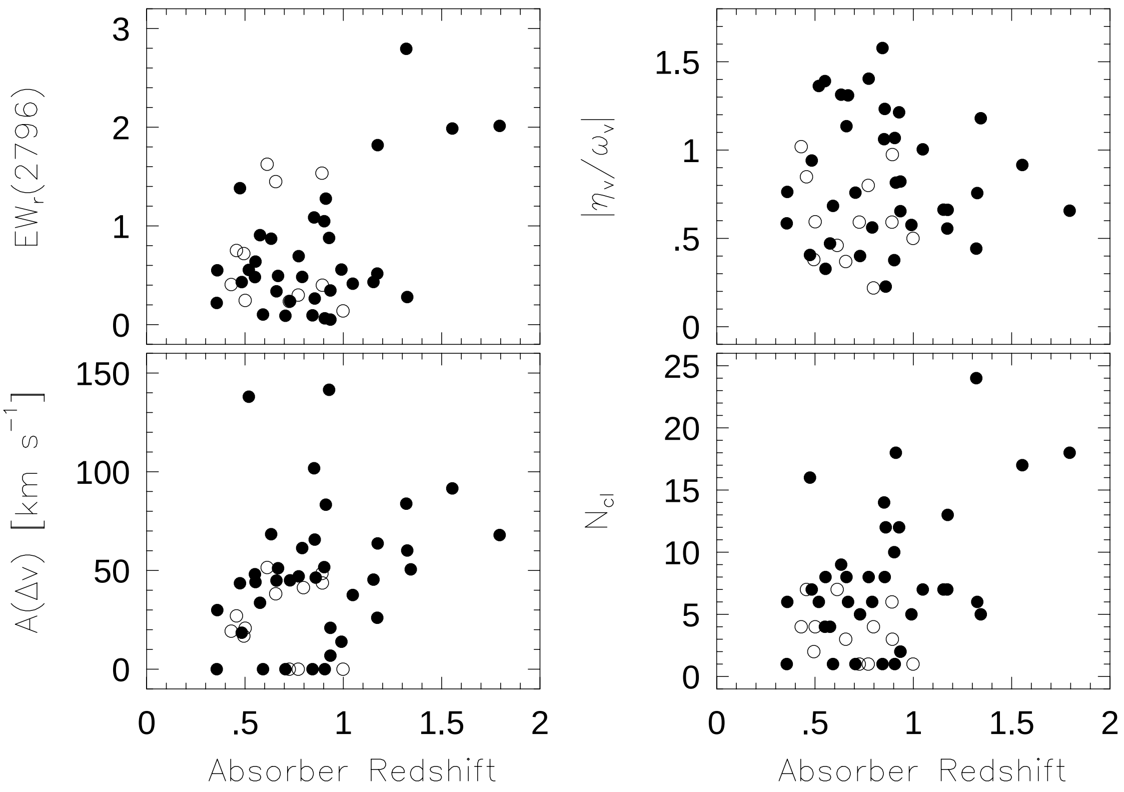

Fig. 3.4.— The redshift distribution of selected overall absorption properties taken from those presented in Table 3.4 — (upper left) the rest–frame equivalent width — (lower left) the median deviation of VP cloud velocities — (upper right) the "shape parameter" — (lower right) the number of clouds per system. The solid points are taken from Sample B and the open points are taken from the full sample (those rejected from Sample B). Based upon Spearman–Kendall tests on Sample B, none of the illustrated absorption properties are inconsistent with no correlation with redshift above the 2σ significance level. The trends that are present are primarily due to the selection of large equivalent width systems at the higher redshifts. Thus, any suggestion of weak correlations in these data likely results from selection effects.

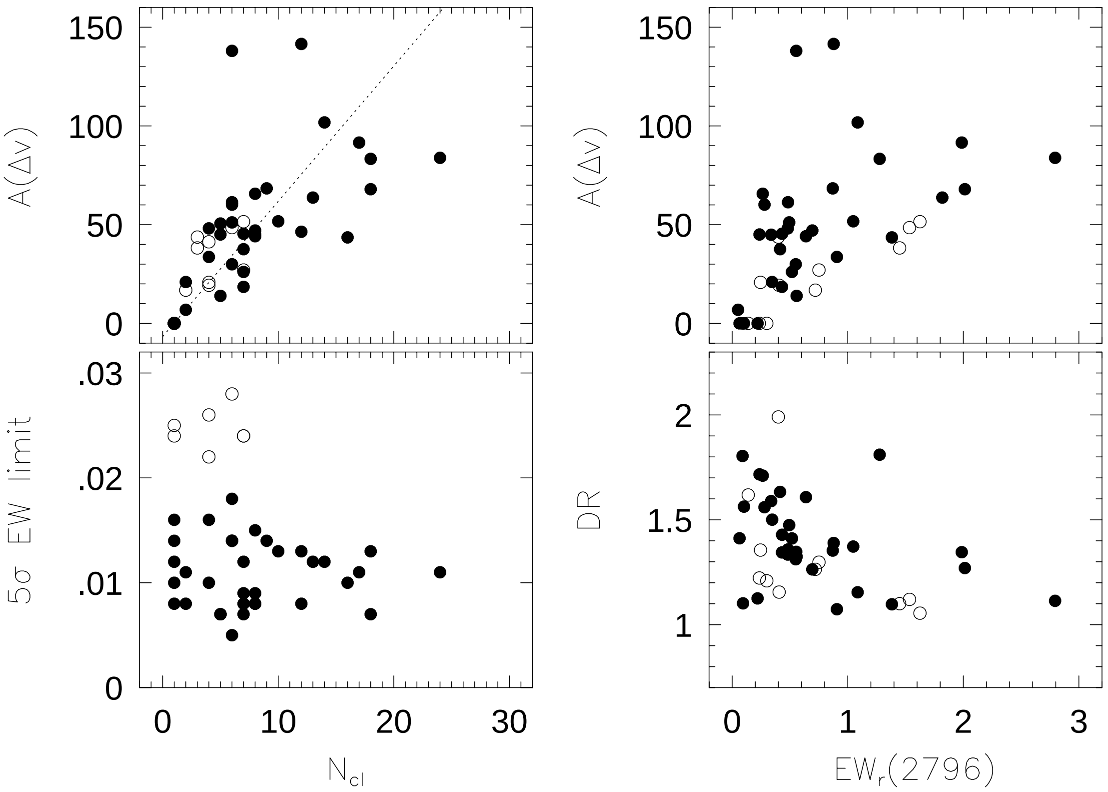

Fig. 3.5.— A small selection of overall absorption properties taken from Table 3.4 to illustrate a range of correlation significance levels — (upper left) the median deviation of VP cloud velocities verses the number of VP clouds — (lower left) the equivalent width detection level verses the number of VP clouds — (upper right) the median deviation of VP cloud velocities verses equivalent width — (lower right) the Mg II doublet ratio verses equivalent width. The solid points are taken from Sample B and the open points are taken from the full sample (those rejected from Sample B). The effects of lower signal to noise ratios on the number of VP components, $N_{\rm cl}$, can be seen in the lower left panel. The dotted line represents a maximum likelihood fit to the "spread" of cloud velocities as a function of the number of clouds. Note that $A(\Delta v) = 0$ at $N_{\rm cl} = 1$ by definition.

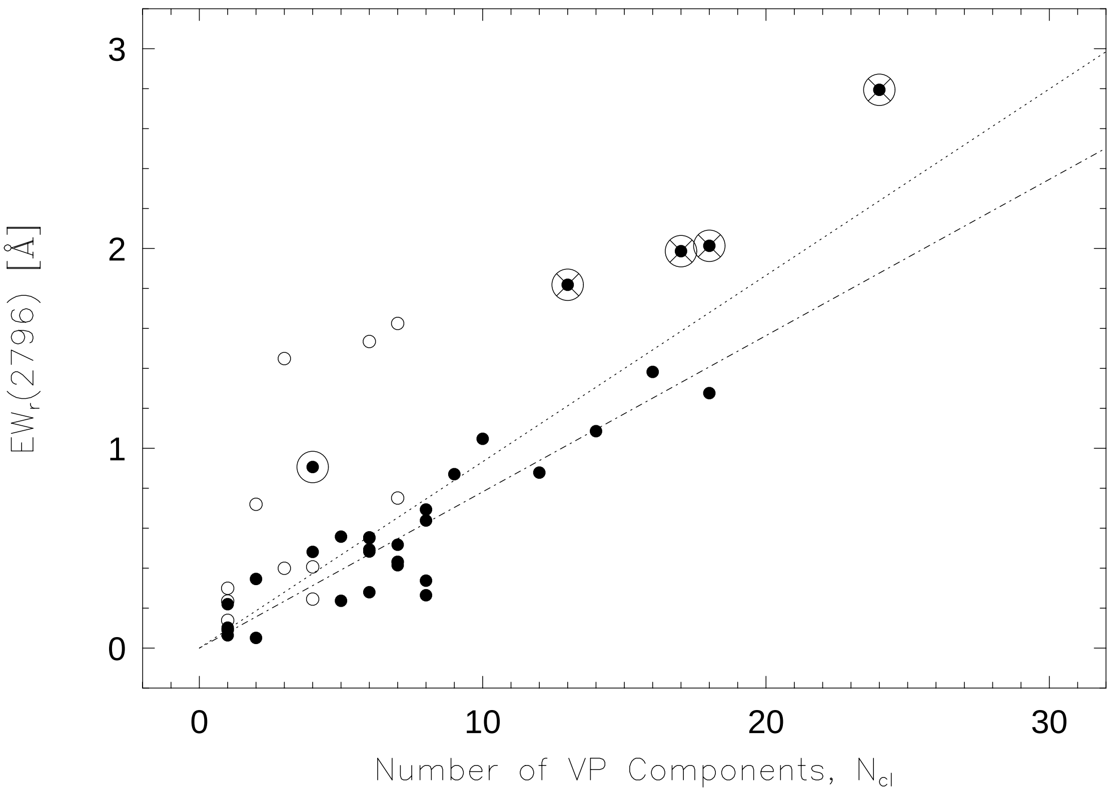

Fig. 3.6.— The Mg II λ2796 equivalent width is strongly correlated to the number of VP components, or clouds. The solid points are taken from Sample B and the open points are taken from the full sample (those rejected from Sample B). The four points with cross hatches are, Q0450 − 132 at $z_{\rm abs} = 1.1746$, Q1213 − 003 at $z_{\rm abs} = 1.5541$, Q1225 + 317 at $z_{\rm abs} = 1.7948$, and Q1213 − 003 at $z_{\rm abs} = 1.3201$, in increasing number of VP components. These systems exhibit highly saturated broad profiles. These four systems were not included in either the maximum likelihood fit (dash–dot) nor the χ^2 minimizing fit (dotted). See text for details. The outlier at (4,0.91) is from the Q0117 + 212 system at $z_{\rm abs} = 0.5764$, which is also a highly saturated profile for which the number of components is likely under estimated.

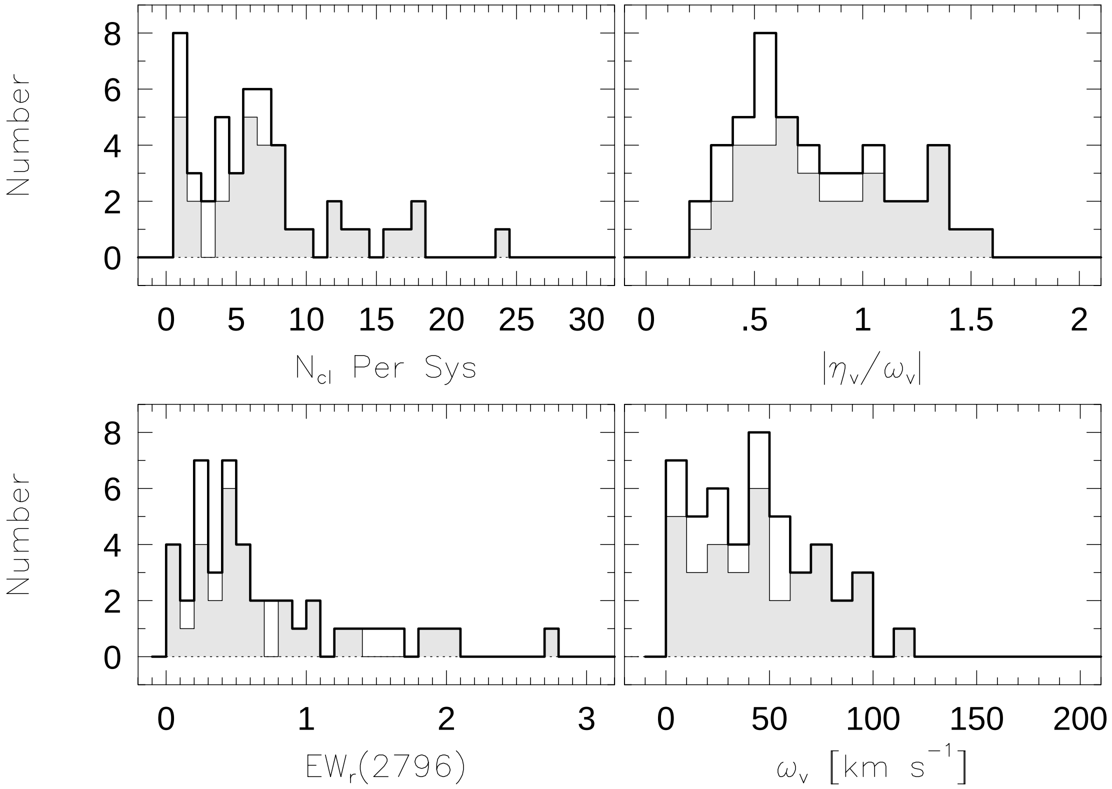

Fig. 3.7.— Histogram distributions of selected overall absorption properties — (upper left) the number of VP components per system — (lower left) the equivalent width — (upper right) the profile asymmetry per unit width (shape parameter) — (lower right) the profile velocity width. The thick line histogram shows the full sample presented in Table 3.1, and the shaded region gives the distribution of Sample B.

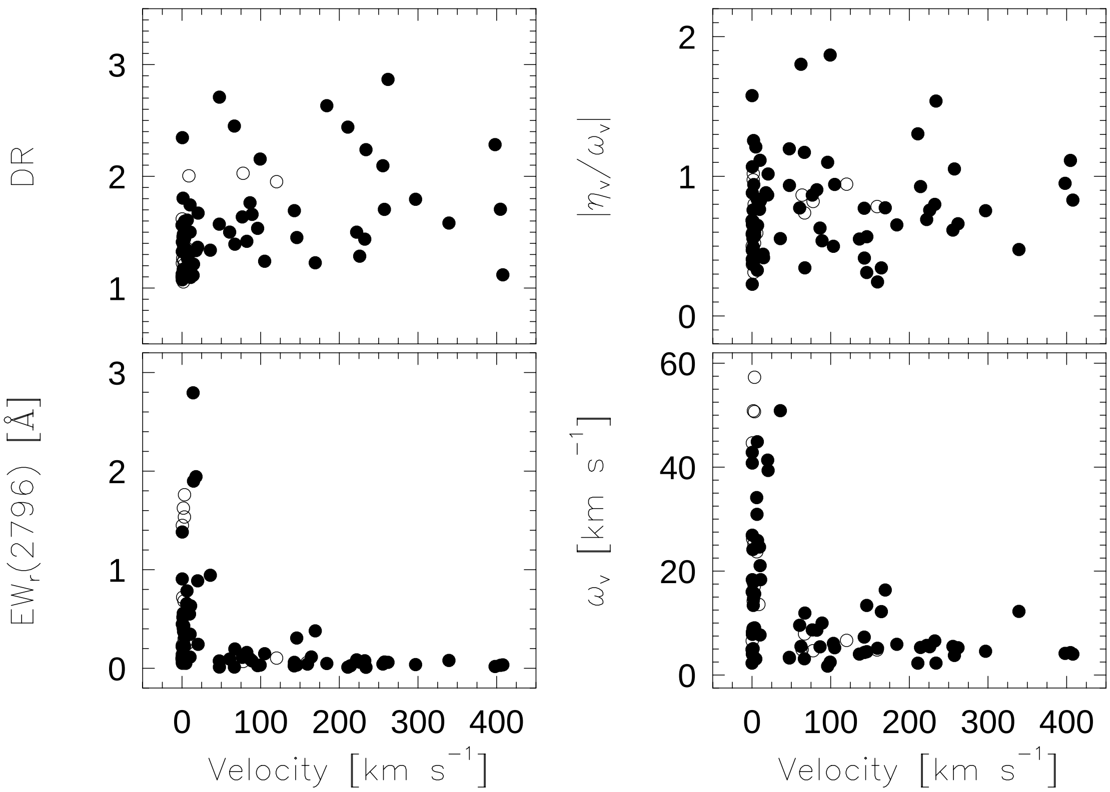

Fig. 3.8.— A selection of subfeature absorption properties verses velocity for which correlation tests were performed (see Table 3.5) — (upper left) the doublet ratio — (lower left) the equivalent width — (upper right) the shape parameter — (lower right) the velocity width. Most telling is the strong clustering of $\omega_v < 10$ km s^{-1} and of EW$_r < 0.2$ Å for $\langle v \rangle > 40$ km s^{-1} (also see Figures 3.10 and 3.11).

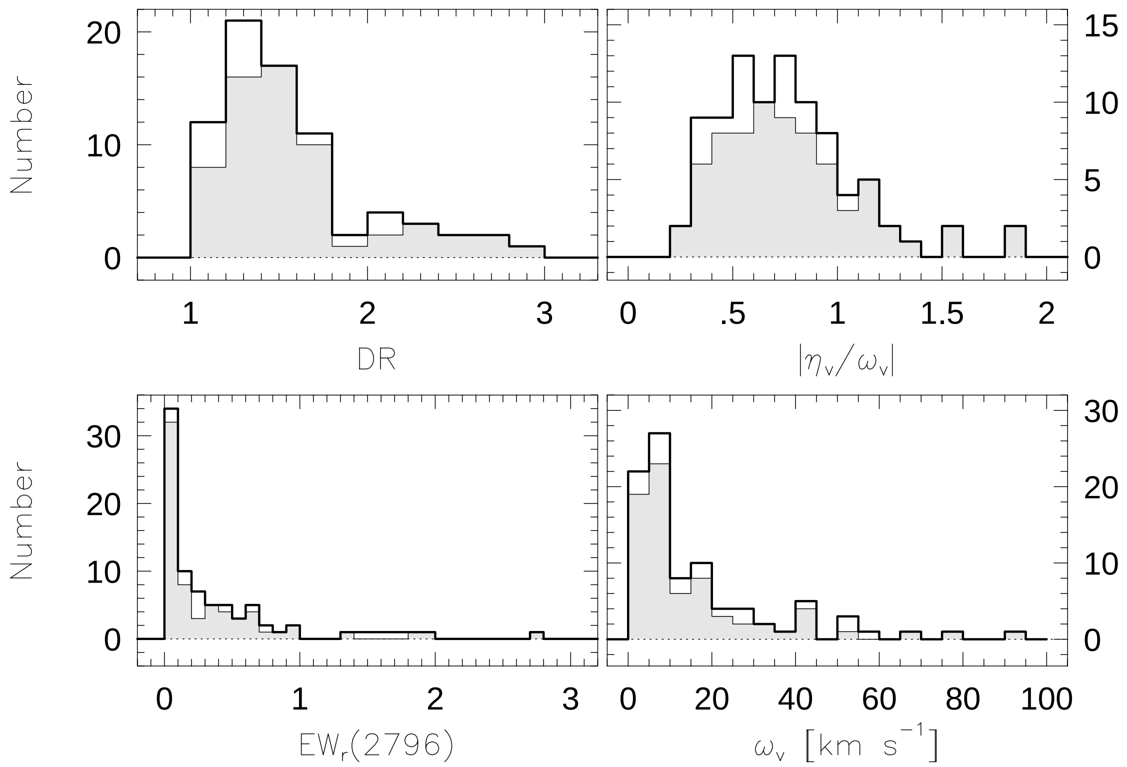

Fig. 3.9.— Histogram distributions of selected subfeature absorption properties — (upper left) the doublet ratios — (lower left) the equivalent widths — (upper right) the subfeature asymmetries per unit width (shape parameter) — (lower right) the subfeature velocity widths. The thick line histogram shows the full sample presented in Table 3.3, and the shaded region gives the distribution of Sample B.

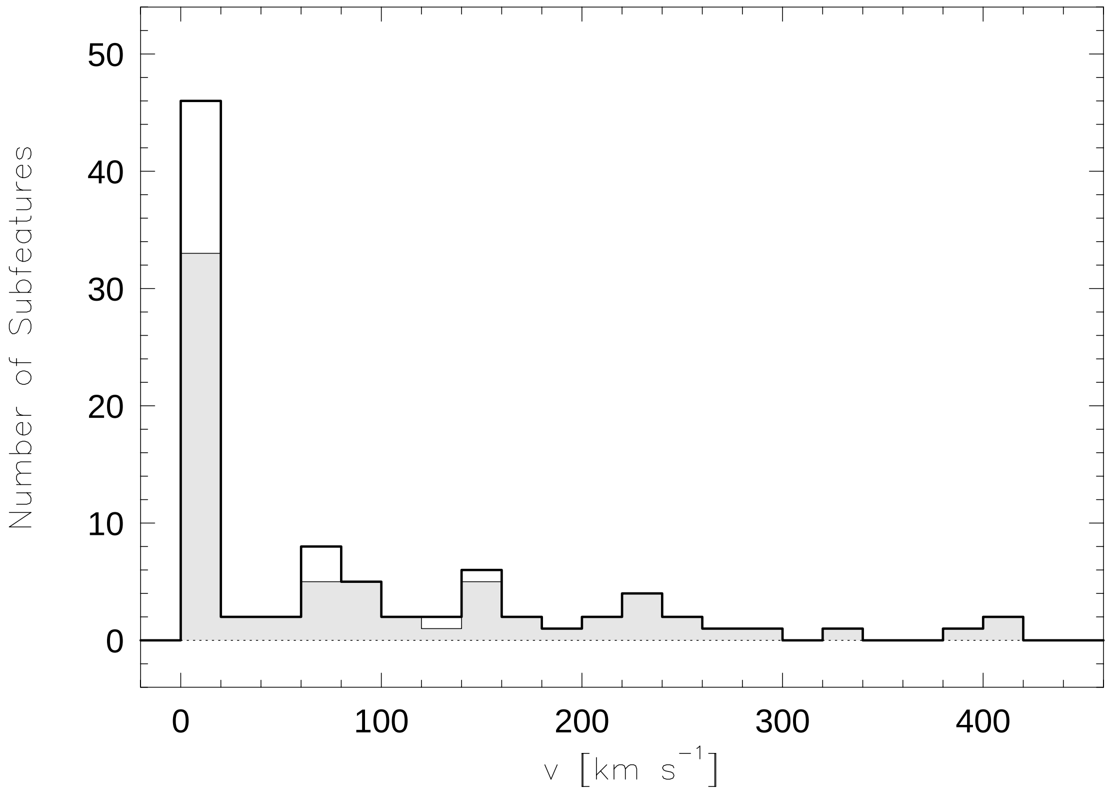

Fig. 3.10.— Histogram distribution giving the number of subfeatures per $\Delta v = 20$ km s^{-1} bin. The thick line histogram shows the full sample presented in Table 3.1, and the shaded region gives the distribution of Sample B. Out of 33 absorption systems, there are 39 subfeatures with $v > 20$ km s^{-1}, from which one can estimate that, on average, there is more than one higher velocity subsystem per absorber with equivalent widths greater than the sample completeness.

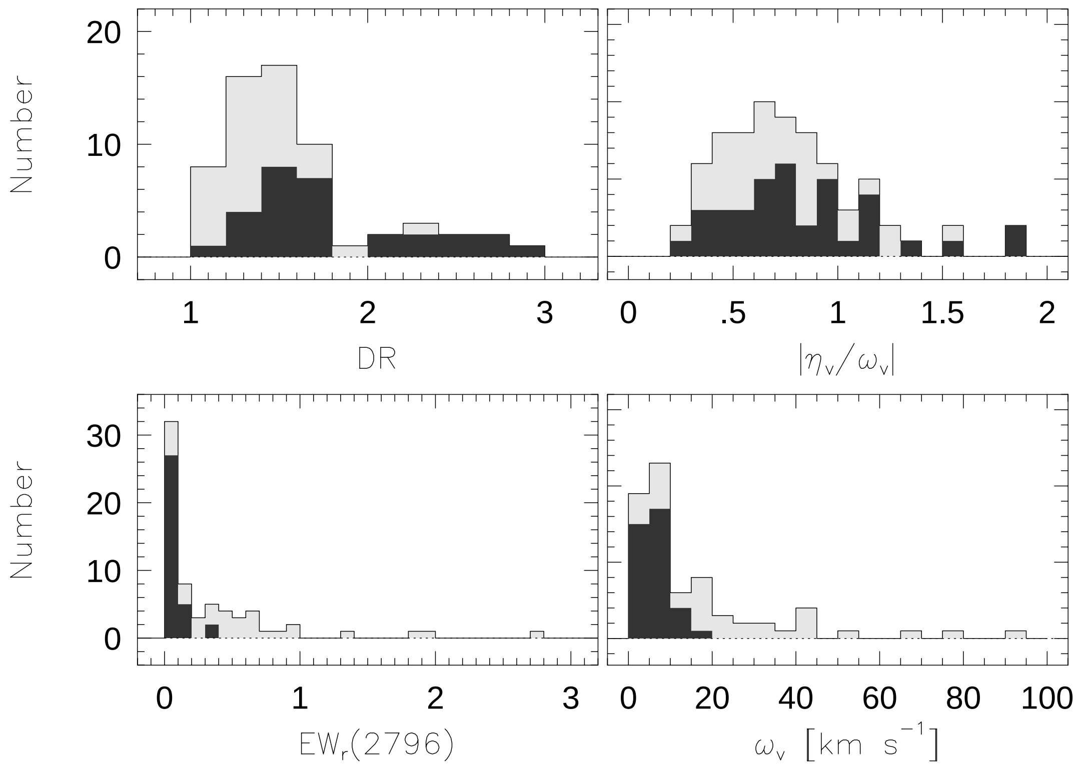

Fig. 3.11.— Based upon the subfeature velocity distribution (see Figure 3.10), the properties of subfeatures with $v > 40$ km s^{-1} were binned as a separate population of absorbers — (upper left) the doublet ratios — (lower left) the equivalent widths — (upper right) the subfeature asymmetries per unit width (shape parameter) — (lower right) the subfeature velocity widths. The lightly shaded histograms are the full Sample B (all velocities) and the solid filled histograms are the $v > 40$ km s^{-1} subpopulation. Though DR greater than two is unphysical, these doublet ratios are suggestive of optically thin gas, where as very few $v > 40$ km s^{-1} subfeatures are optically thick.

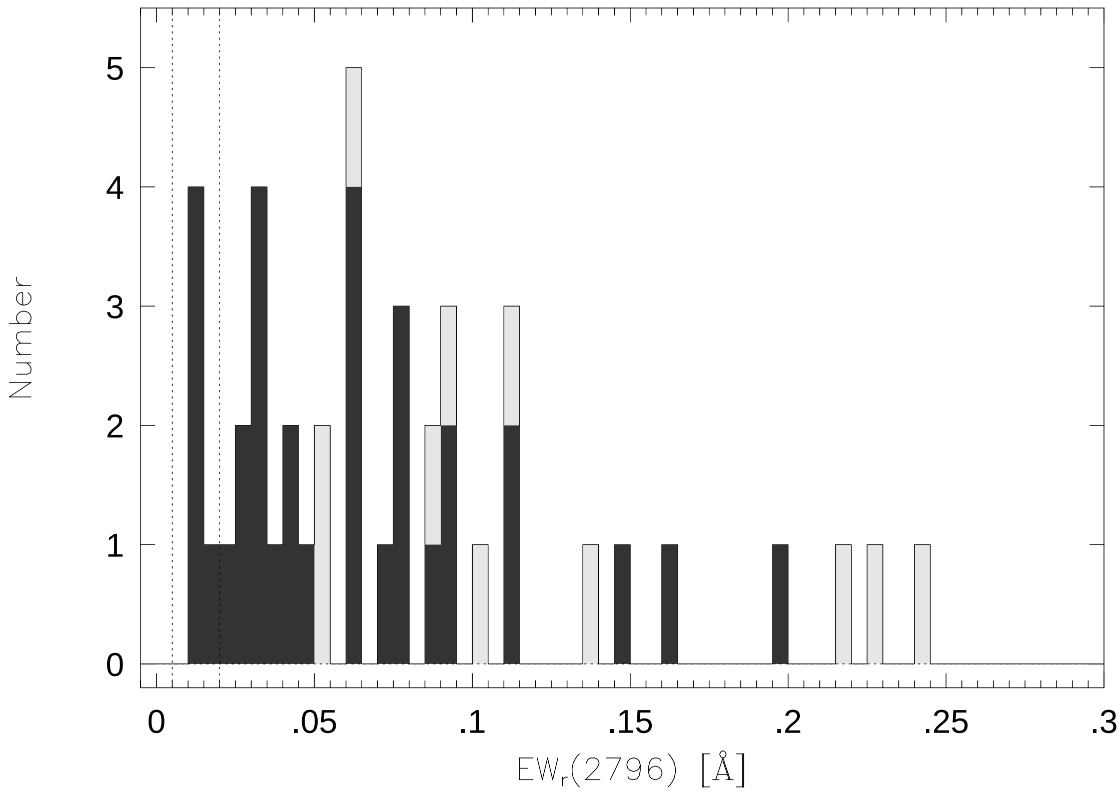

Fig. 3.12.— The subfeature rest–frame equivalent widths binned at ΔEW$_r$ = 0.005 Å. The region of partial completeness (0.005 $\leq$ EW$_r$ $\leq$ 0.02 Å) is marked by the vertical dotted lines. The lightly shaded histogram is the full Sample B (all velocities) and the solid filled histogram is the $v > 40$ km s^{-1} subpopulation. Note that all EW$_r$ $\leq$ 0.05 Å subfeatures have $v > 40$ km s^{-1}. Though the statistics are small, there is no clear evidence for an EW$_r$ cutoff of so called "satellite" lines in Mg II absorption systems. This is particularly evident in view of the fact that, for EW$_r$ $\leq$ 0.02 Å, the sample is not complete.

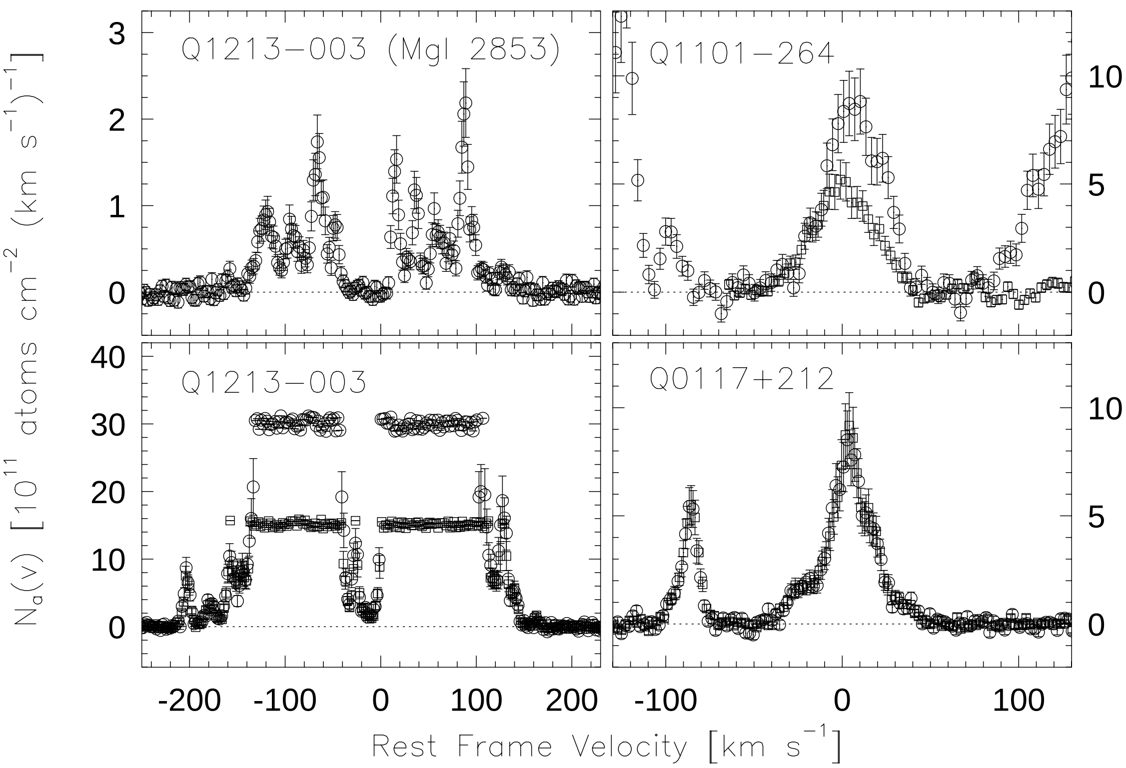

Fig. 3.13.— The apparent column densities, $N_a(v)$ for three selected systems. The left two panels are $N_a(v)$ for the Mg I transition (upper) and for the Mg II doublet (lower) from the Q1213 − 003 at $z_{\rm abs} = 1.3201$ system. The upper right panel is the Mg II doublet from the Q1101 − 264 at $z_{\rm abs} = 0.3563$ system, and the lower right panel shows Mg II from the Q0117 + 212 at $z_{\rm abs} = 1.0479$ system. The error bars are the 1σ uncertainties. For the Mg II doublets, open circles are the $\lambda2803$ transition and boxes are the $\lambda2796$ transition. The uncertainties are not shown for the saturated pixels, which give a lower limit to $N_a(v)$. Note the discrepancy in the Q1101 − 264 profiles. The $\lambda2803$ transition is likely blended with a Ly α absorption line.

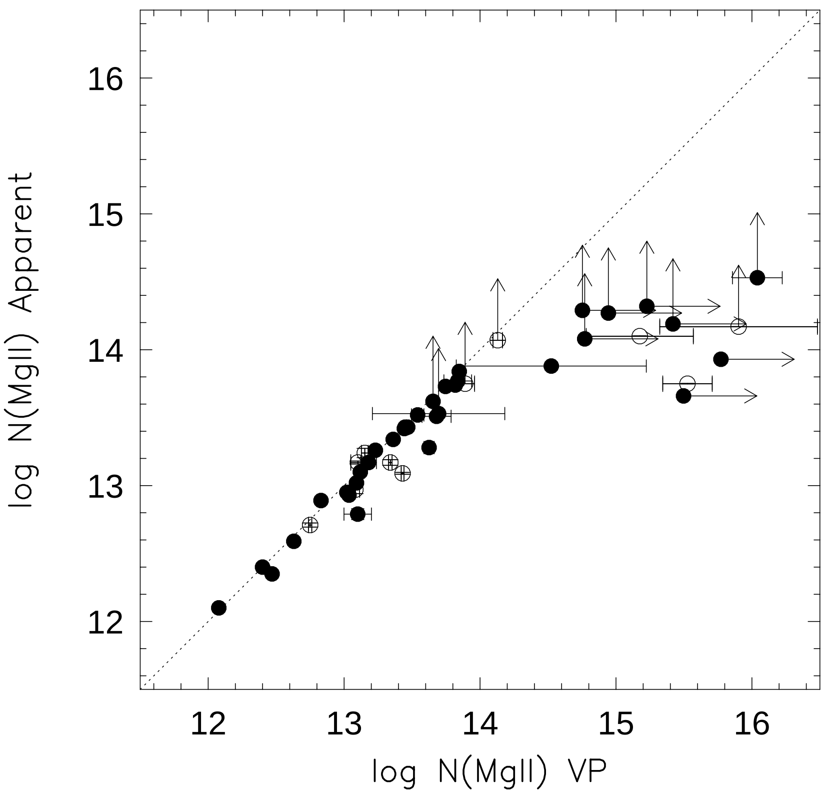

Fig. 3.14.— The full Mg II $\lambda 2796$ profile apparent column densities verses the VP decomposition column densities (see Table 3.2). The solid points are taken from Sample B and the open points are taken from the full sample (those rejected from Sample B). The formal uncertainties are shown, but are often the size of the data points. Lower limits are given by the arrows (for the VP column densities, a lower limit is shown in the case where the fractional error is ≥ 1). There is a clear breakdown of the correlation at a VP column density of $\log N \sim 14.5$ cm^{-2}, corresponding to an apparent column density where unresolved saturation sets in, $\log N_a \sim 13.5$ cm^{-2}.

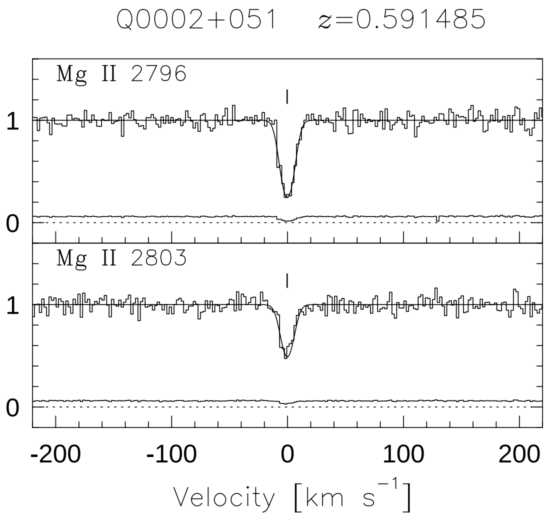

Fig. 3.15.— $Q0002+051$ at $z = 0.5915$: Absorption profiles and Voigt Profile fits.

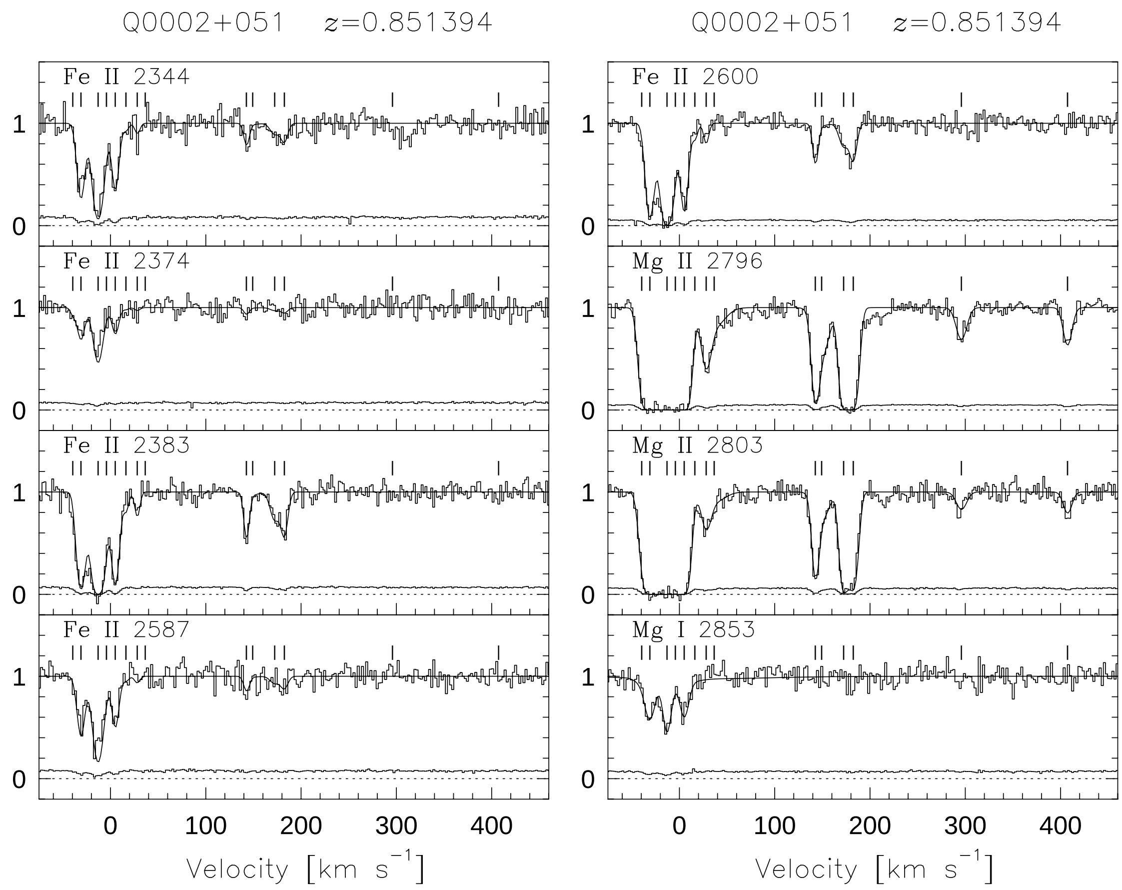

Fig. 3.16.— $Q0002+051$ at $z = 0.8514$: Absorption profiles and Voigt Profile fits.

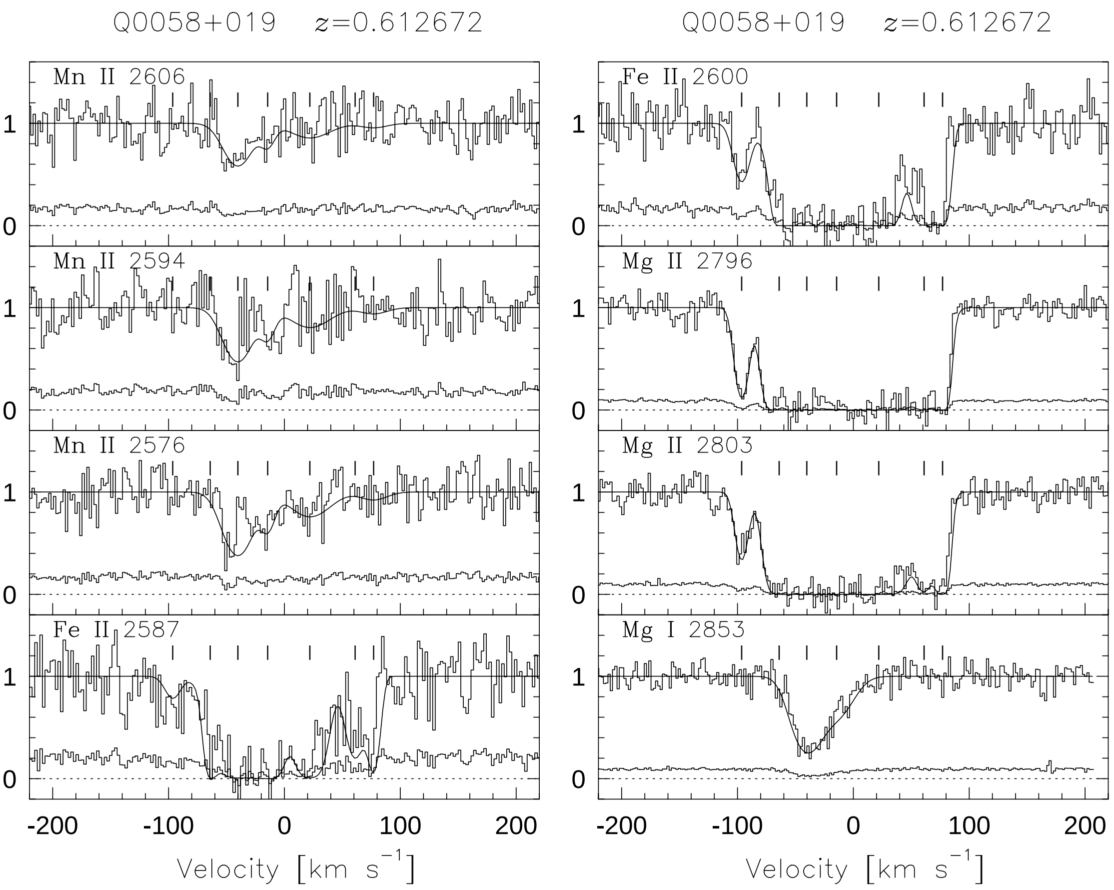

Fig. 3.17.— $Q0058+019$ at $z = 0.6127$: Absorption profiles and Voigt Profile fits.

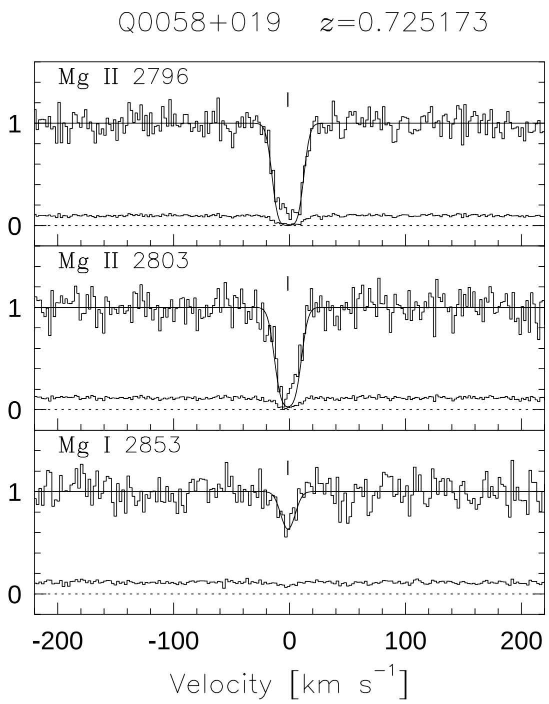

Fig. 3.18.— Q0058 + 019 at $z = 0.7252$: Absorption profiles and Voigt Profile fits.

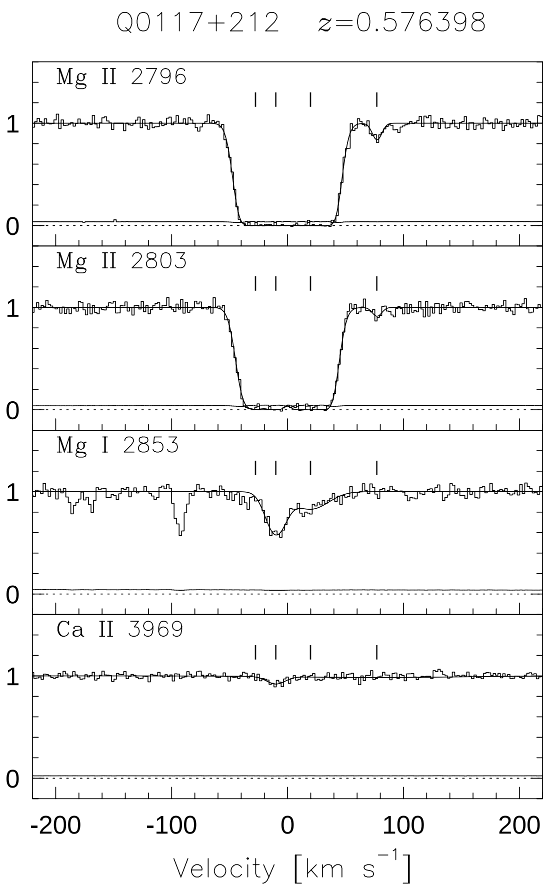

Fig. 3.19.— $Q0117 + 212$ at $z = 0.5764$: Absorption profiles and Voigt Profile fits.

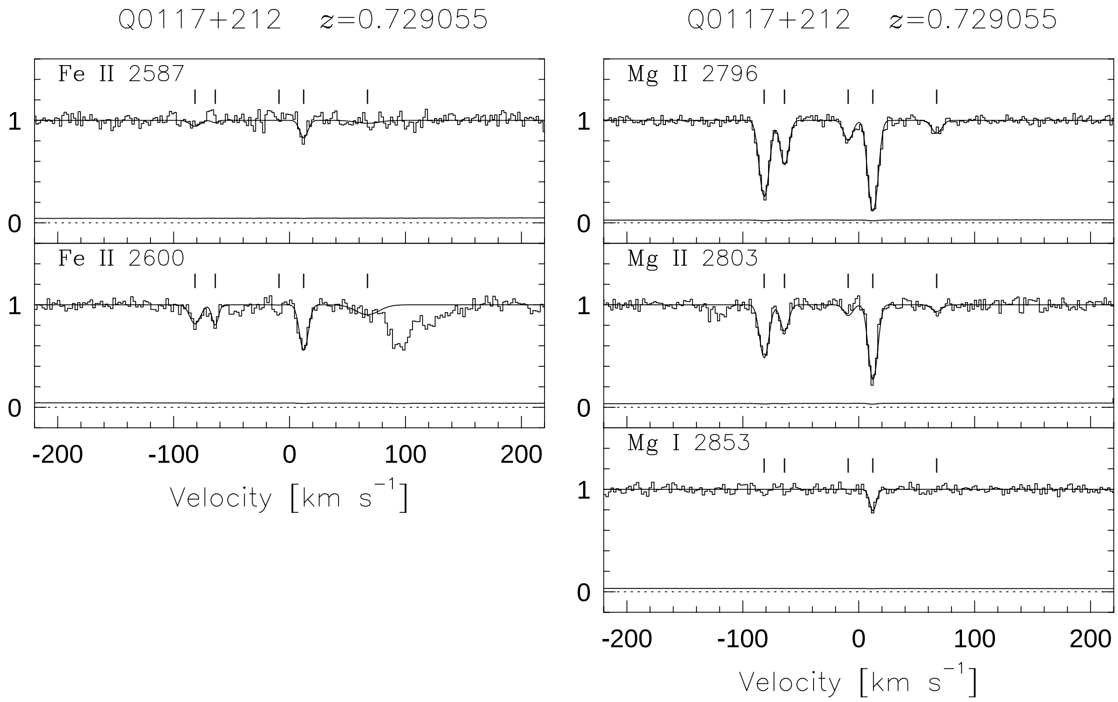

Fig. 3.20.— $Q0117+212$ at $z = 0.7291$: Absorption profiles and Voigt Profile fits.

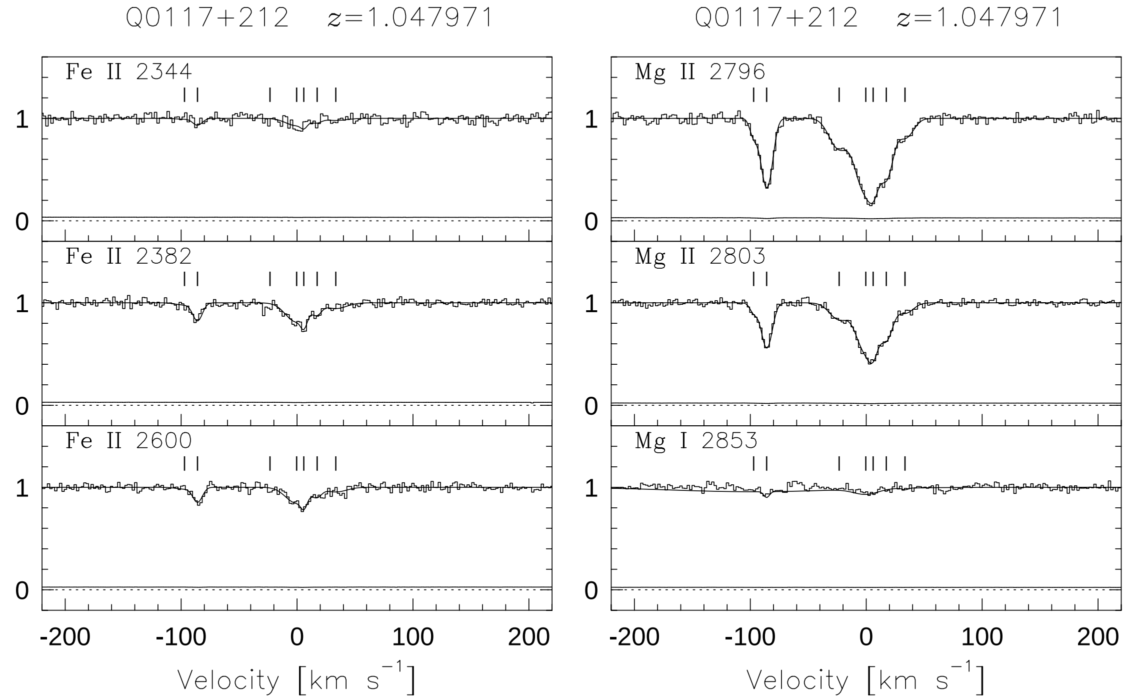

Fig. 3.21.— $Q0117 + 212$ at $z = 1.0480$: Absorption profiles and Voigt Profile fits.

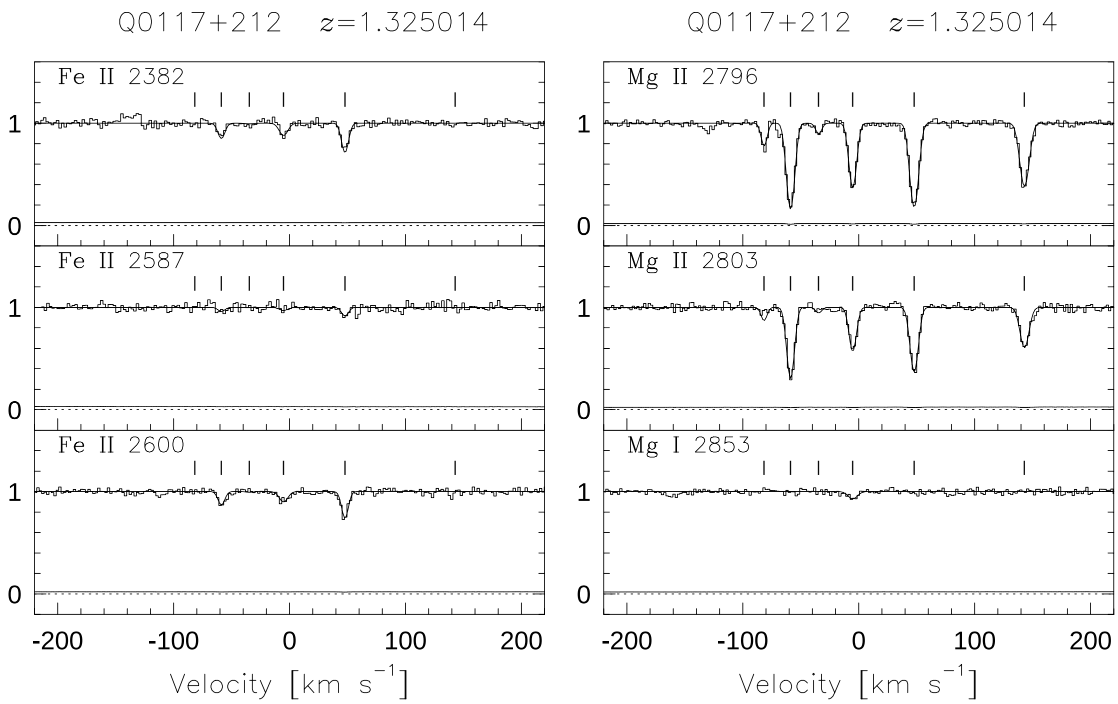

Fig. 3.22.— $Q0117+212$ at $z = 1.3250$: Absorption profiles and Voigt Profile fits.

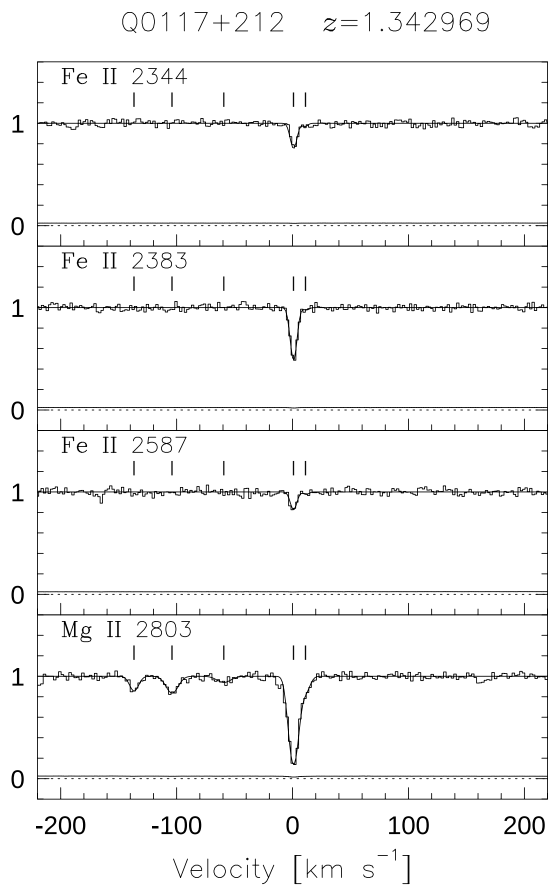

Fig. 3.23.— $Q0117+212$ at $z = 1.3430$: Absorption profiles and Voigt Profile fits.

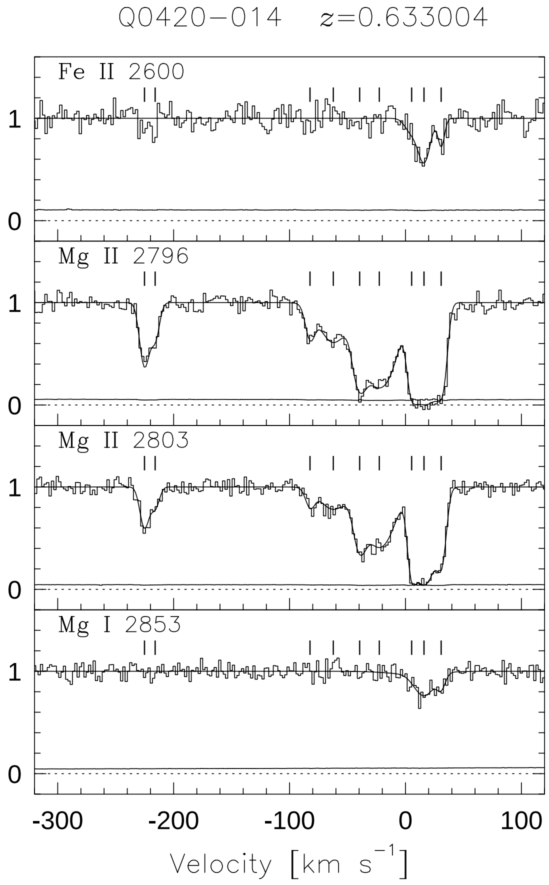

Fig. 3.24.— Q0420 − 014 at $z = 0.6330$: Absorption profiles and Voigt Profile fits.

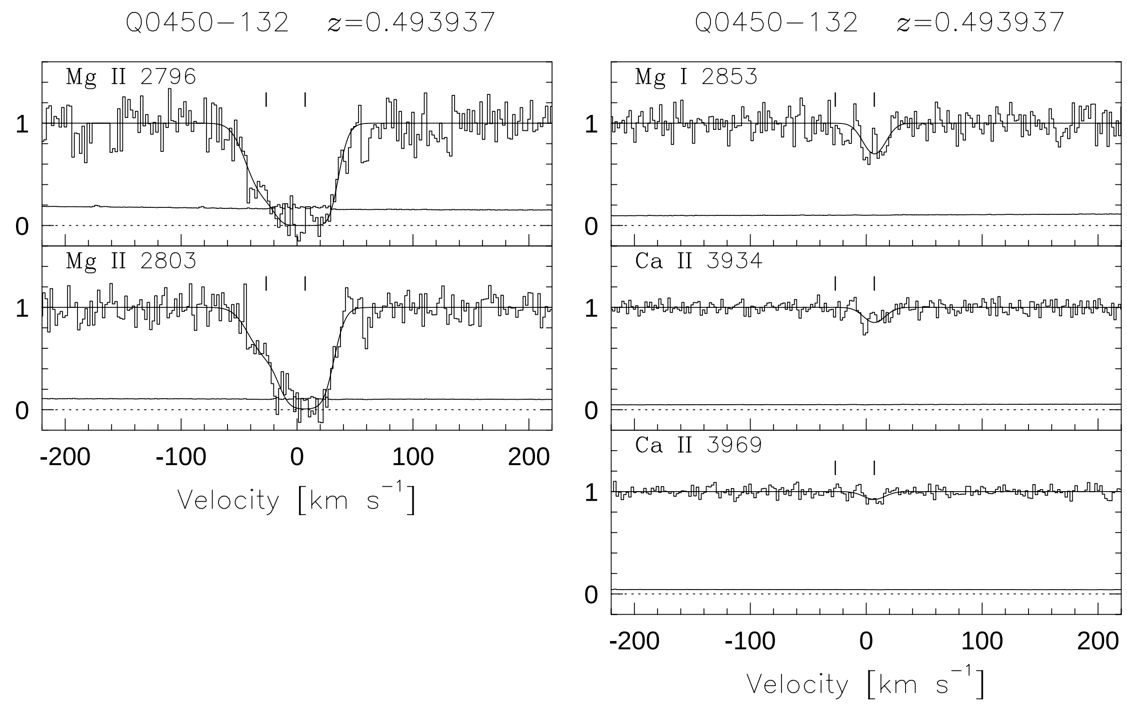

Fig. 3.25.— Q0450 − 132 at $z = 0.4939$: Absorption profiles and Voigt Profile fits.

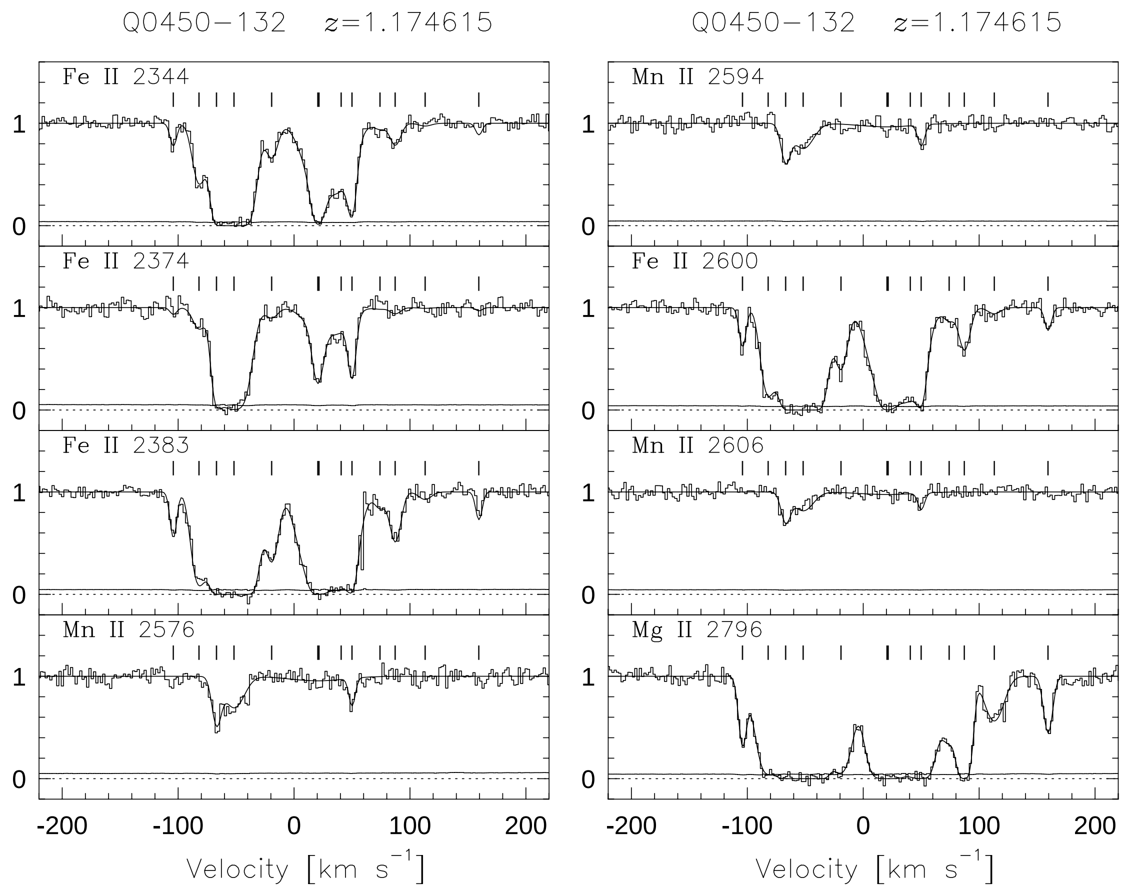

Fig. 3.26.— Q0450 − 132 at $z = 1.1746$: Absorption profiles and Voigt Profile fits.

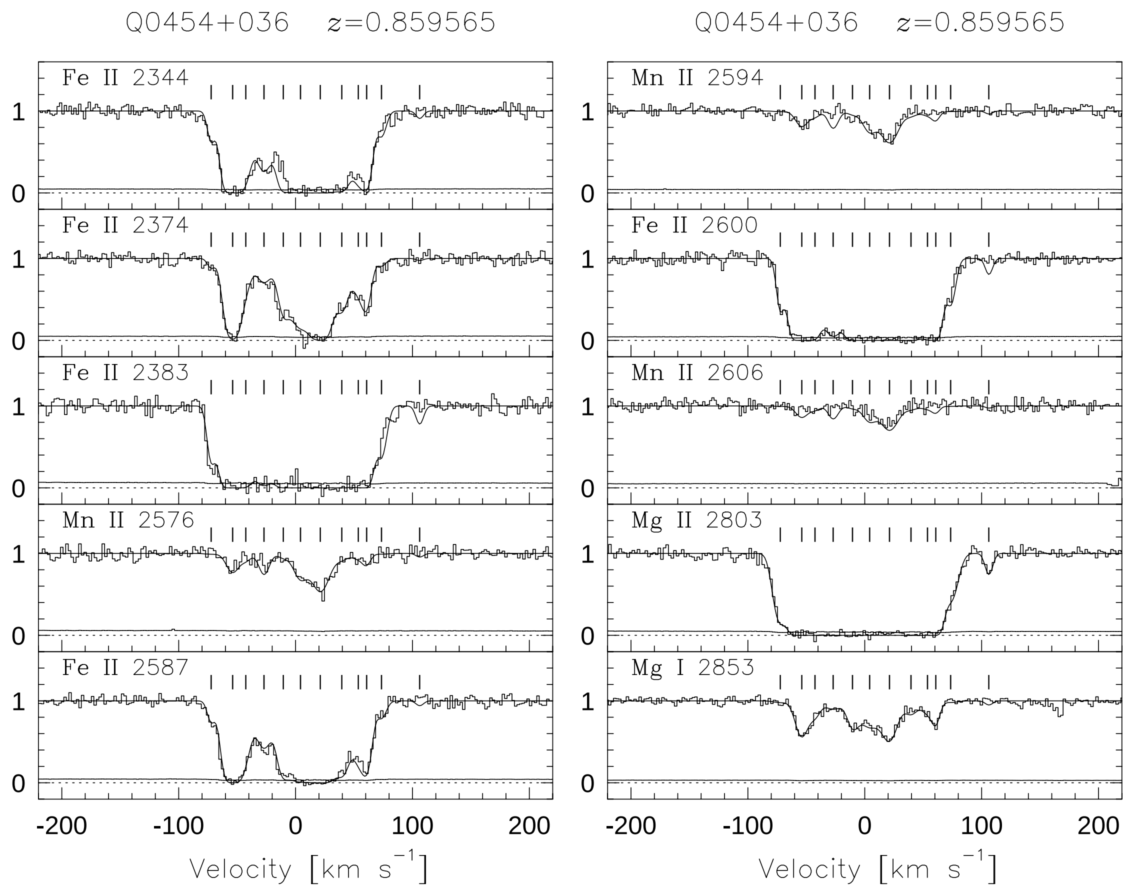

Fig. 3.27.— $Q0454+036$ at $z = 0.8596$: Absorption profiles and Voigt Profile fits.

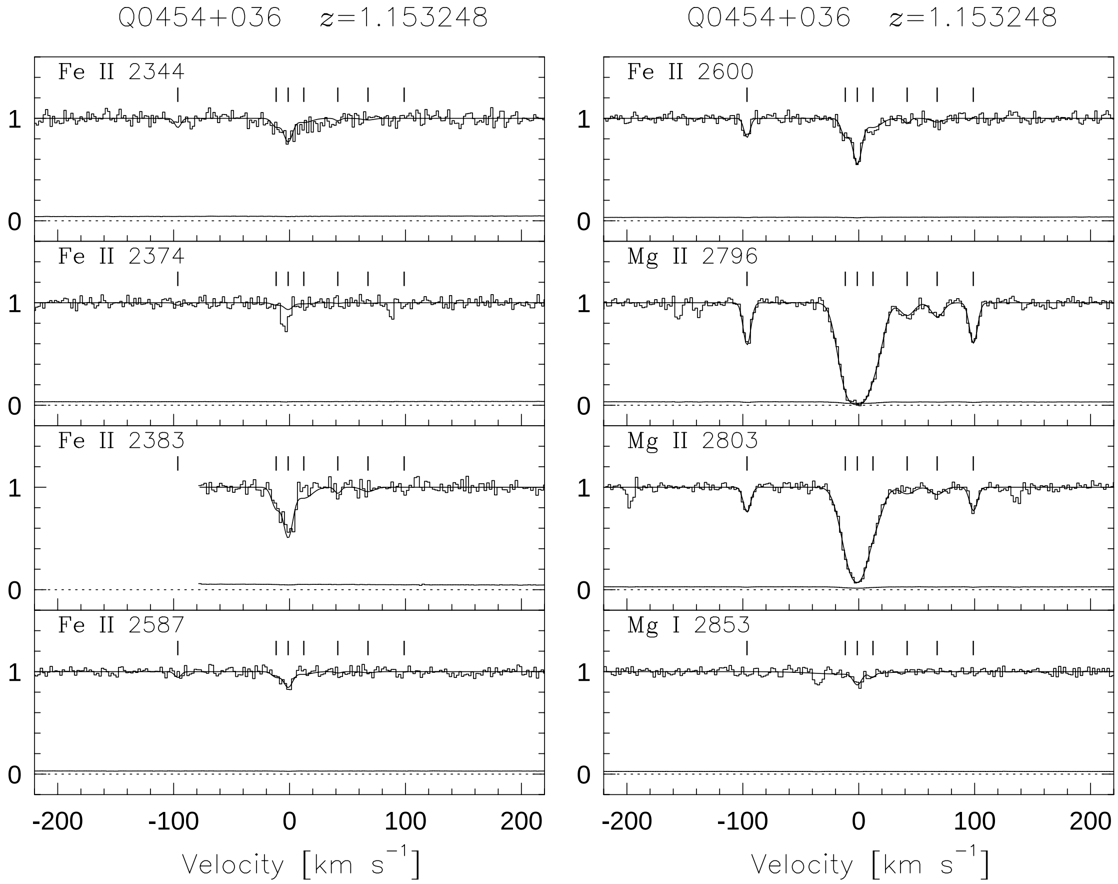

Fig. 3.28.— Q0454 + 036 at $z = 1.1533$: Absorption profiles and Voigt Profile fits.

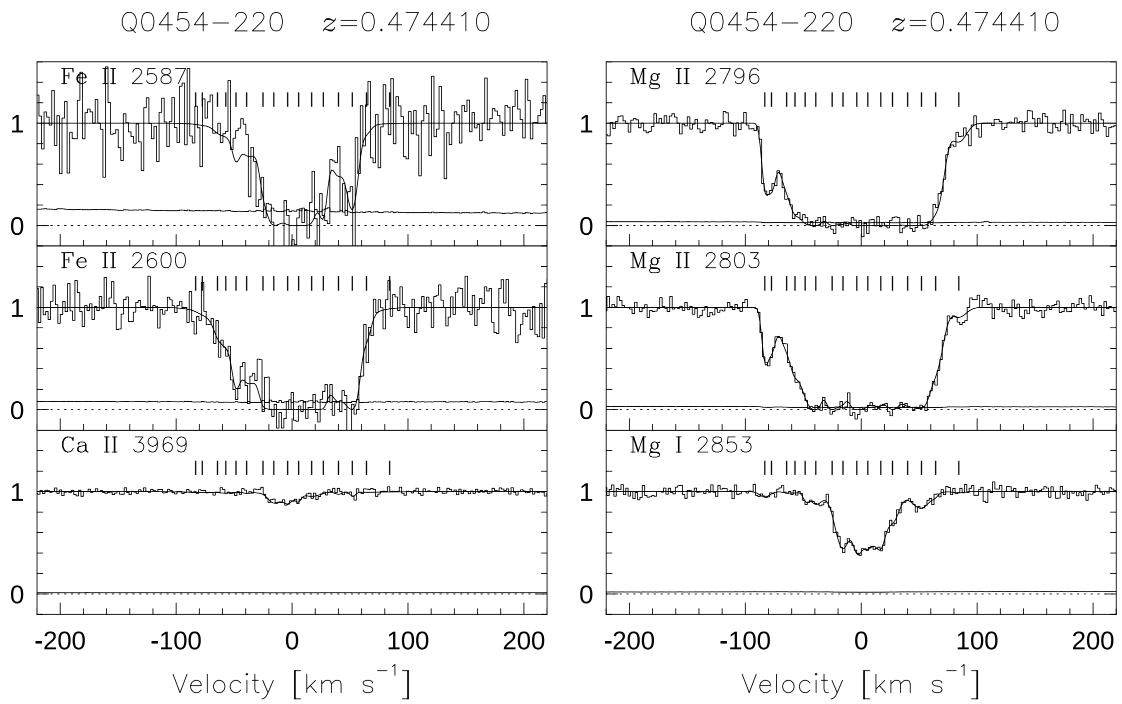

Fig. 3.29.— Q0454 − 220 at $z = 0.4744$: Absorption profiles and Voigt Profile fits.

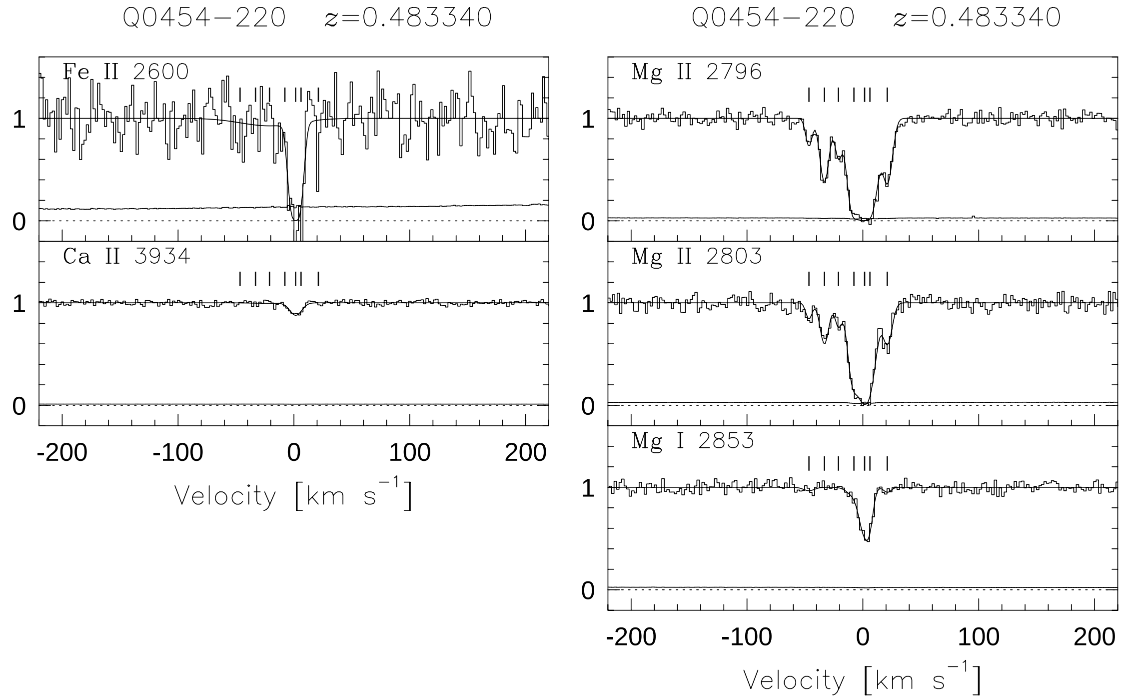

Fig. 3.30.— Q0454 − 220 at $z = 0.4833$: Absorption profiles and Voigt Profile fits.

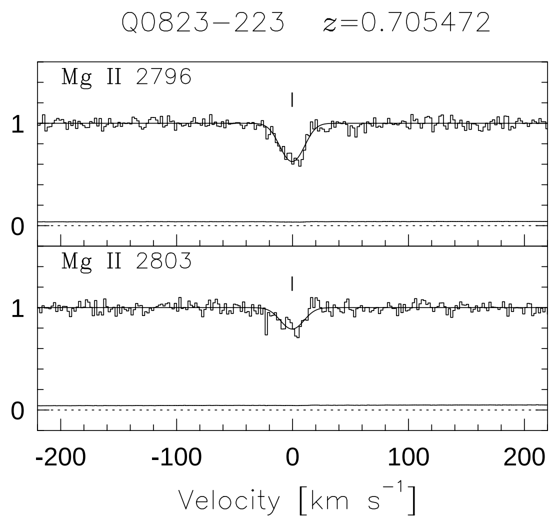

Fig. 3.31.— Q0823 − 223 at $z = 0.7055$: Absorption profiles and Voigt Profile fits.

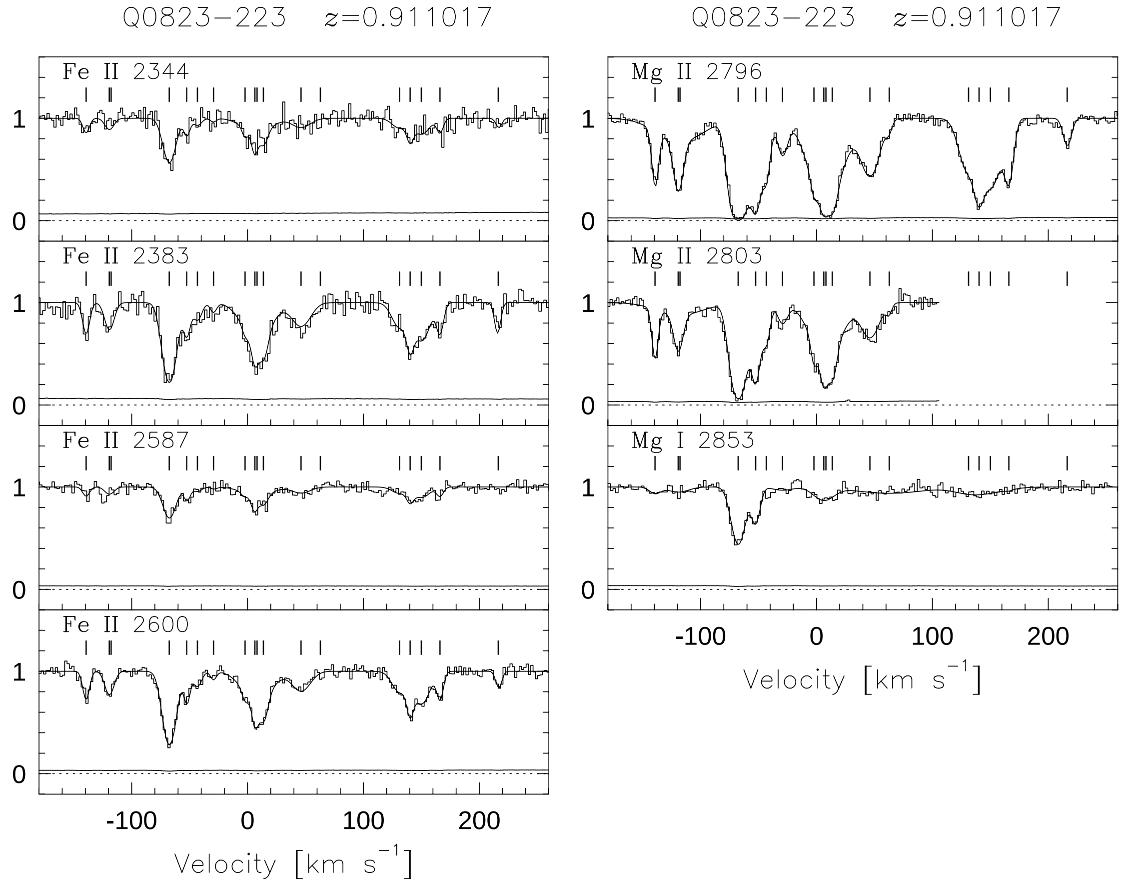

Fig. 3.32.— Q0823 − 223 at $z = 0.9110$: Absorption profiles and Voigt Profile fits.

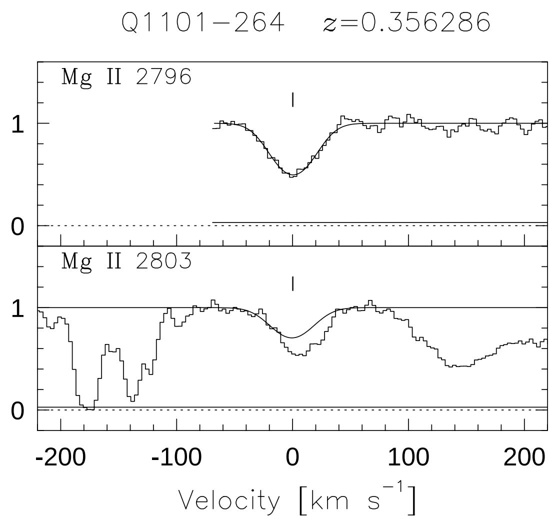

Fig. 3.33.— Q1101 − 264 at $z = 0.3563$: Absorption profiles and Voigt Profile fits.

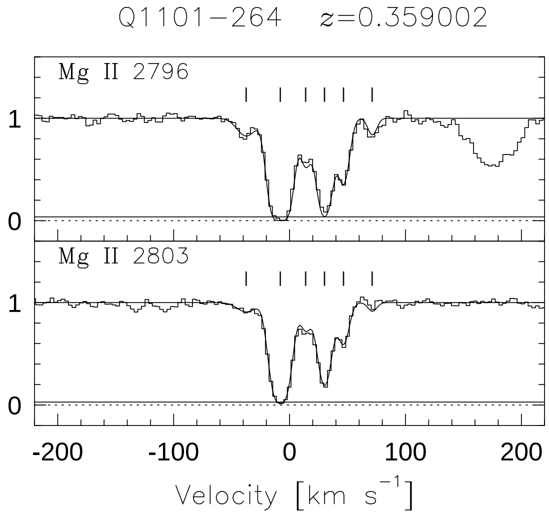

Fig. 3.34.— Q1101 − 264 at $z = 0.3590$: Absorption profiles and Voigt Profile fits.

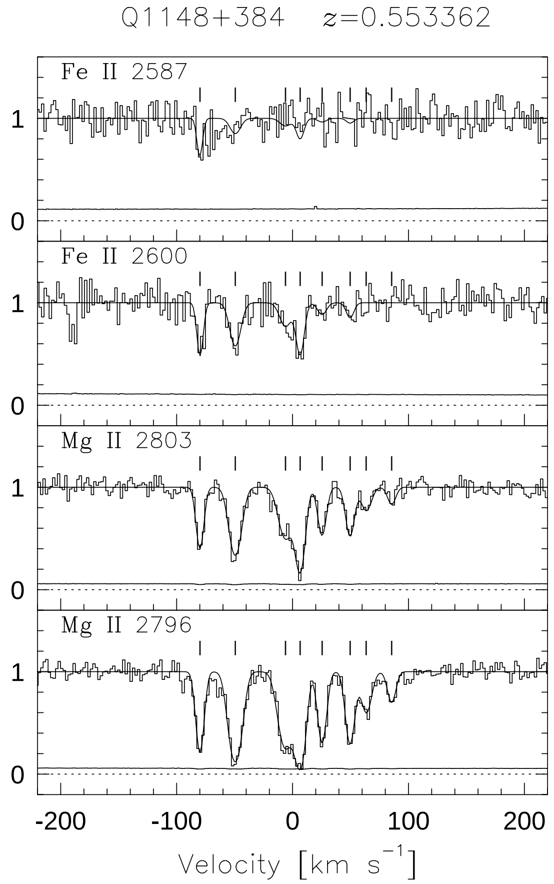

Fig. 3.35.— $Q1148+384$ at $z = 0.5534$: Absorption profiles and Voigt Profile fits.

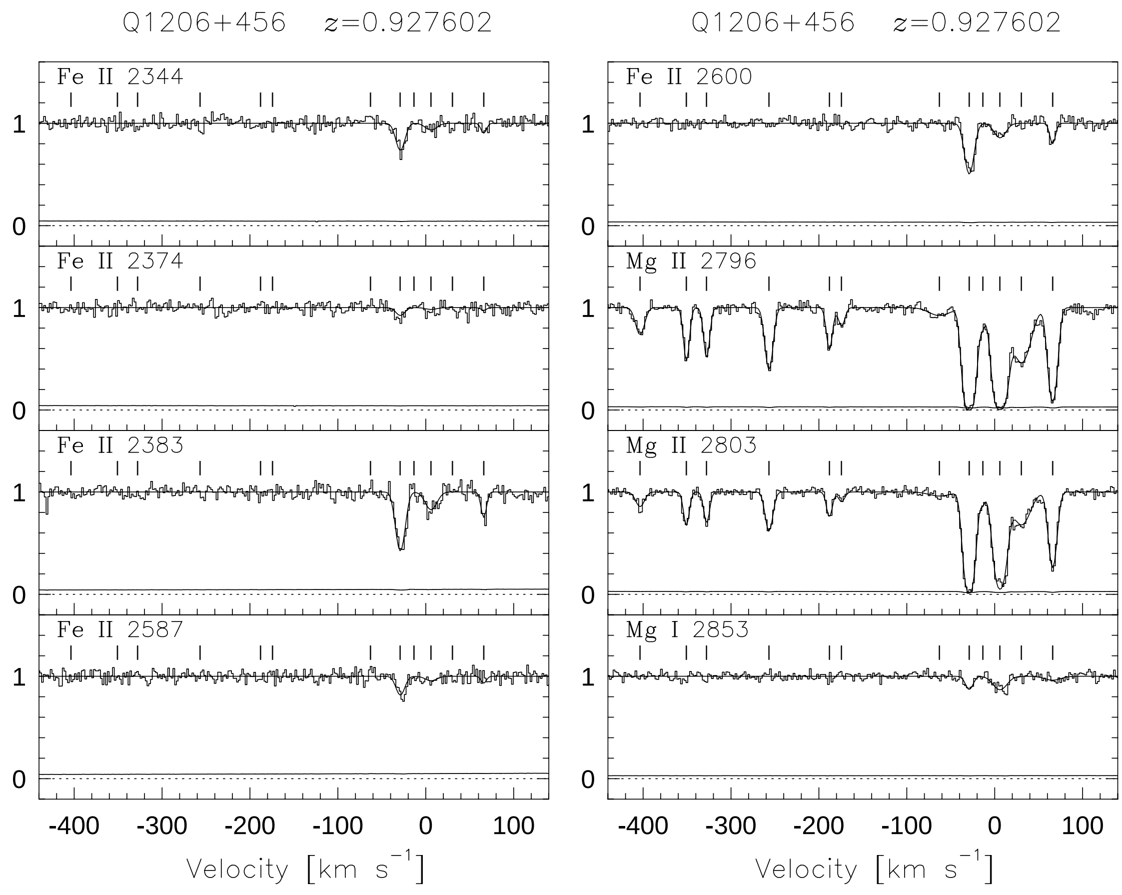

Fig. 3.36.— $Q1206+456$ at $z = 0.9276$: Absorption profiles and Voigt Profile fits.

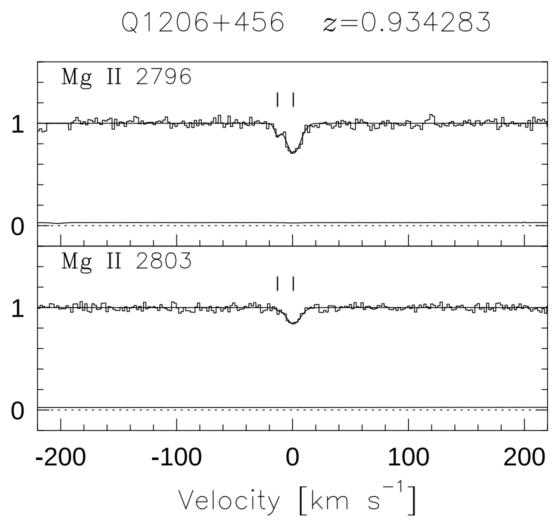

Fig. 3.37.— Q1206 + 456 at $z = 0.9343$: Absorption profiles and Voigt Profile fits.

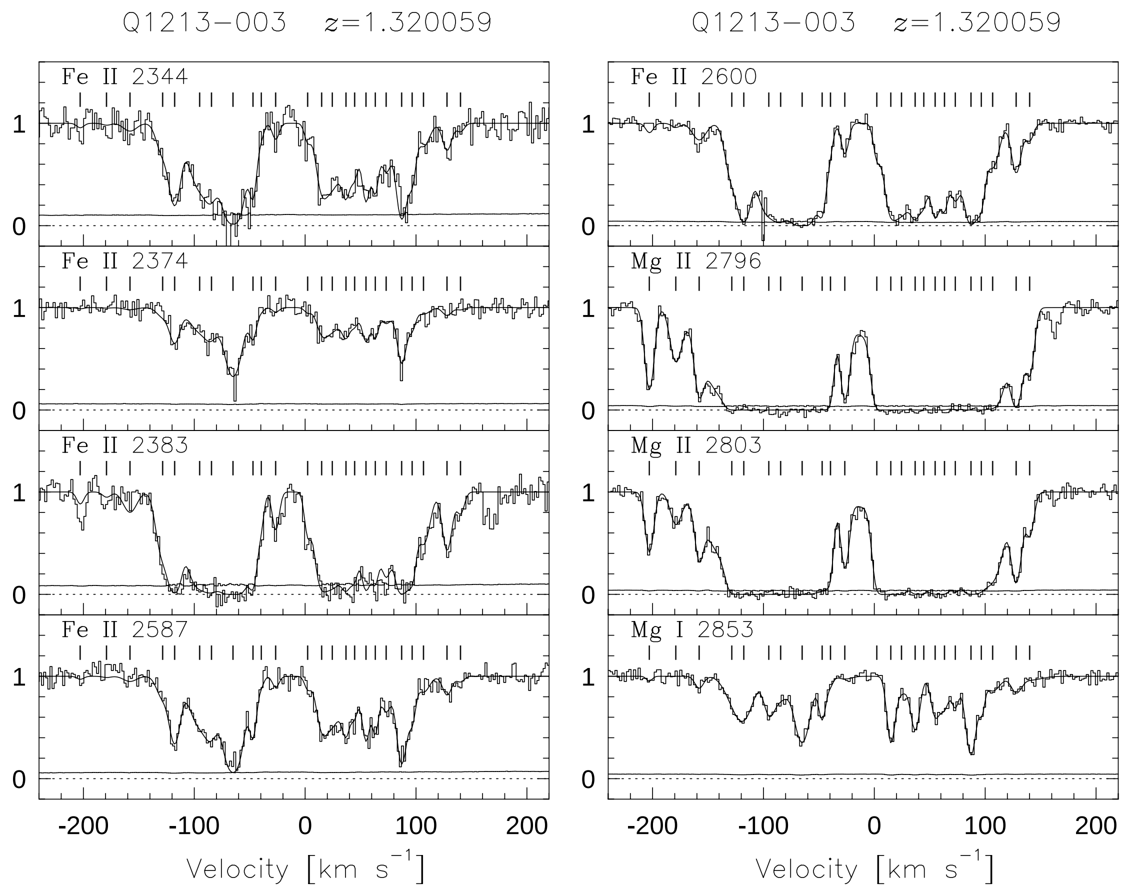

Fig. 3.38.— Q1213 − 003 at $z = 1.3200$: Absorption profiles and Voigt Profile fits.

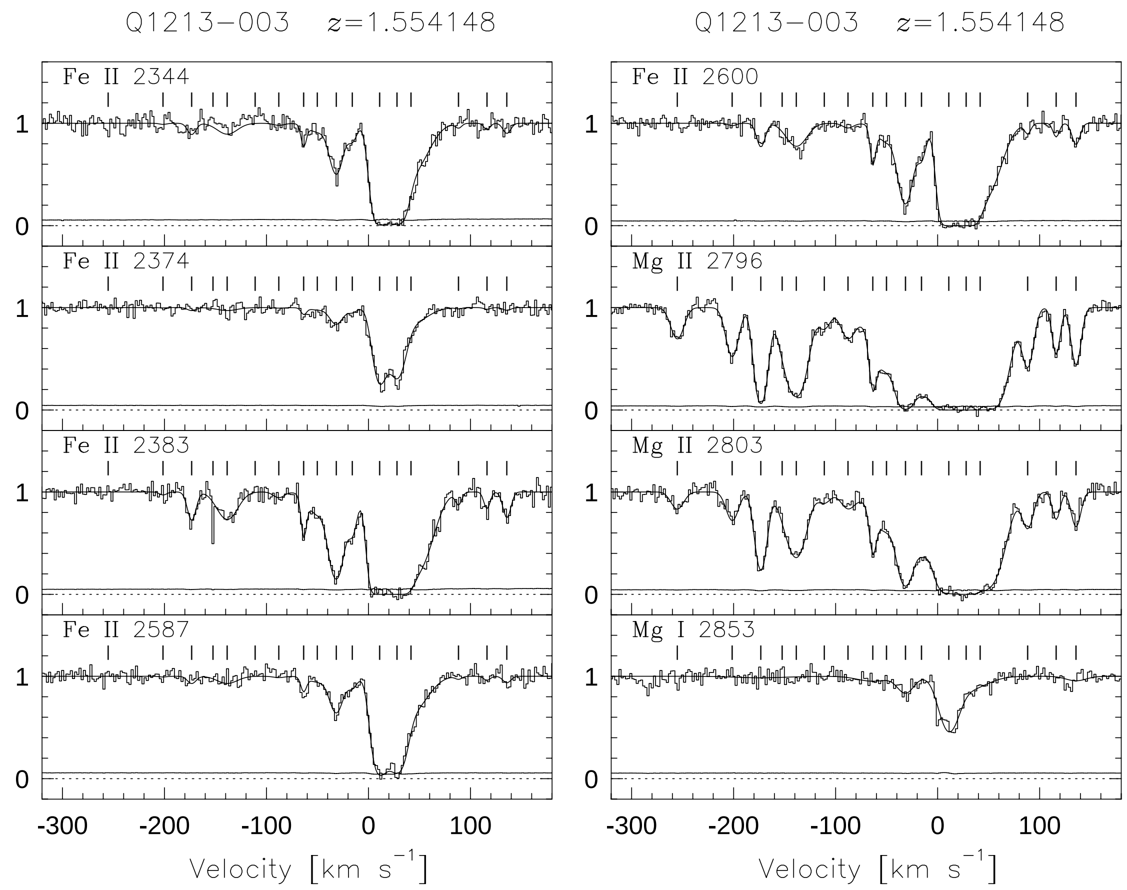

Fig. 3.39.— Q1213 − 003 at $z = 1.5541$: Absorption profiles and Voigt Profile fits.

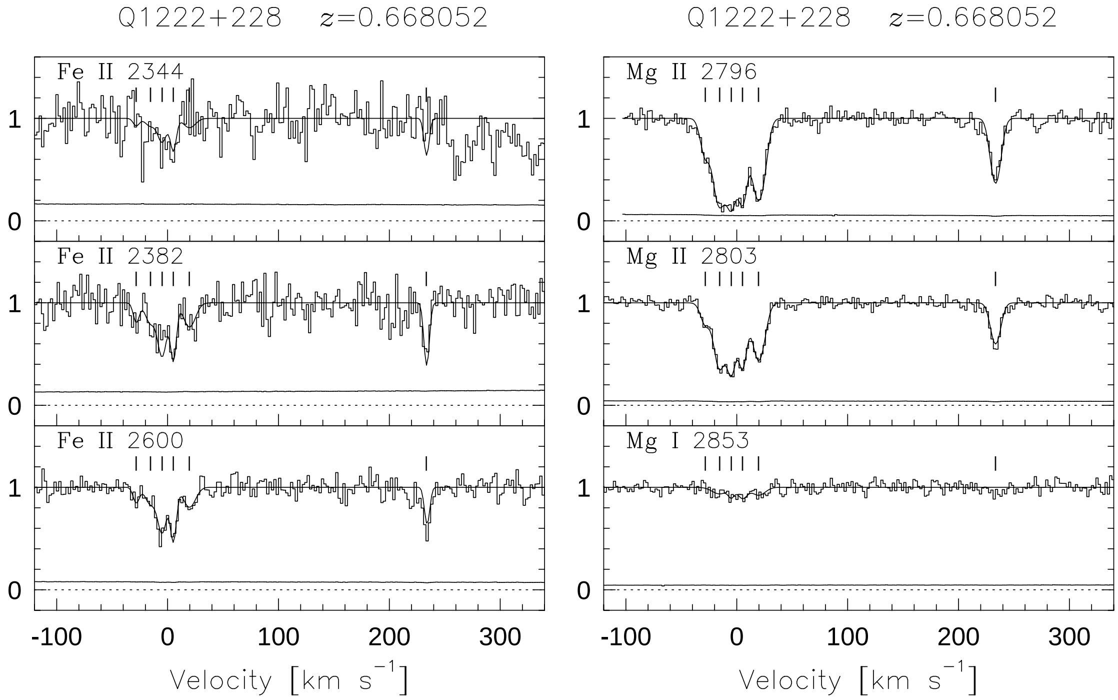

Fig. 3.40.— $Q1222+228$ at $z = 0.6681$: Absorption profiles and Voigt Profile fits.

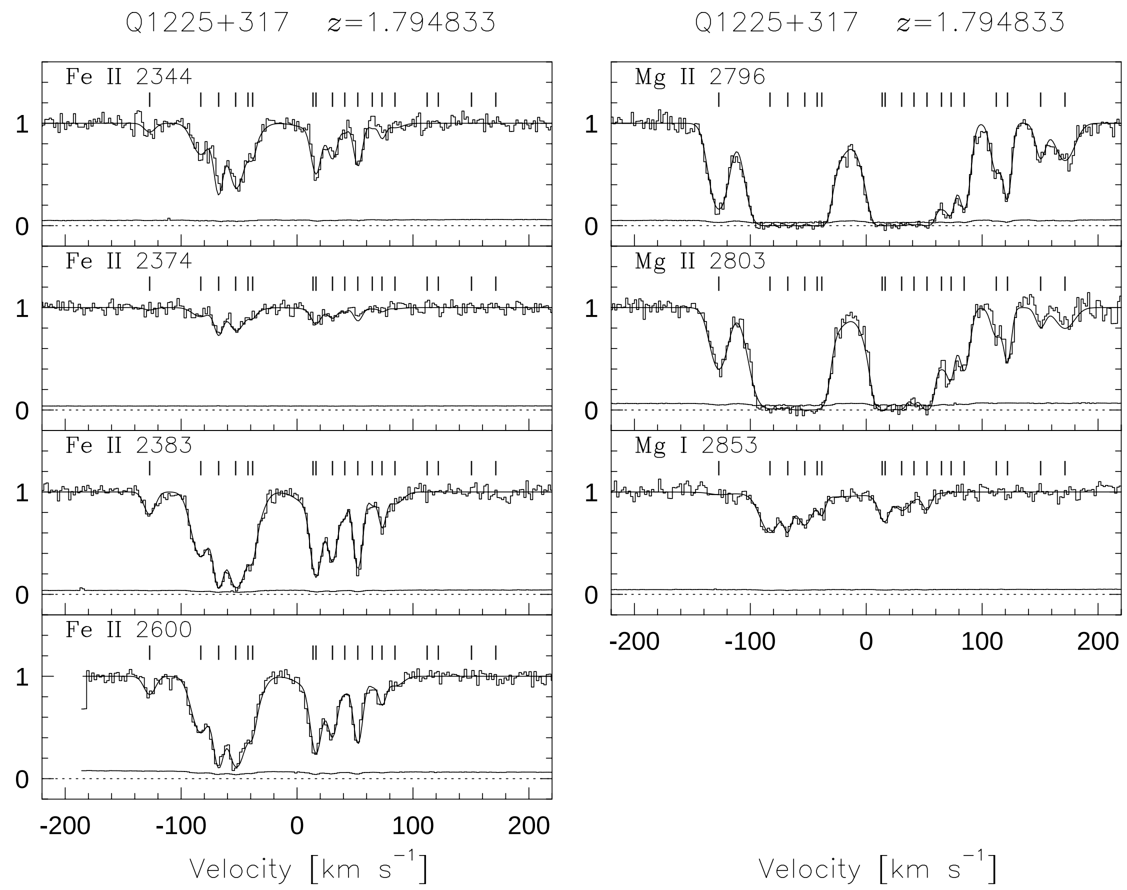

Fig. 3.41.— $Q1225+317$ at $z = 1.7948$: Absorption profiles and Voigt Profile fits.

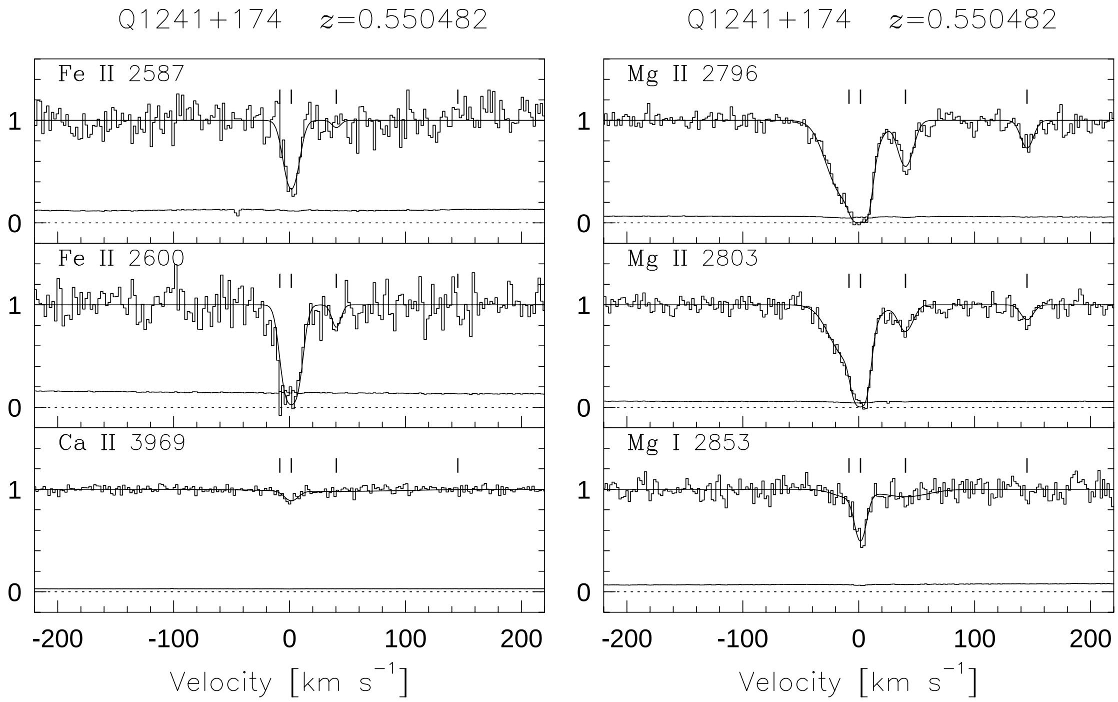

Fig. 3.42.— $Q1241 + 174$ at $z = 0.5505$: Absorption profiles and Voigt Profile fits.

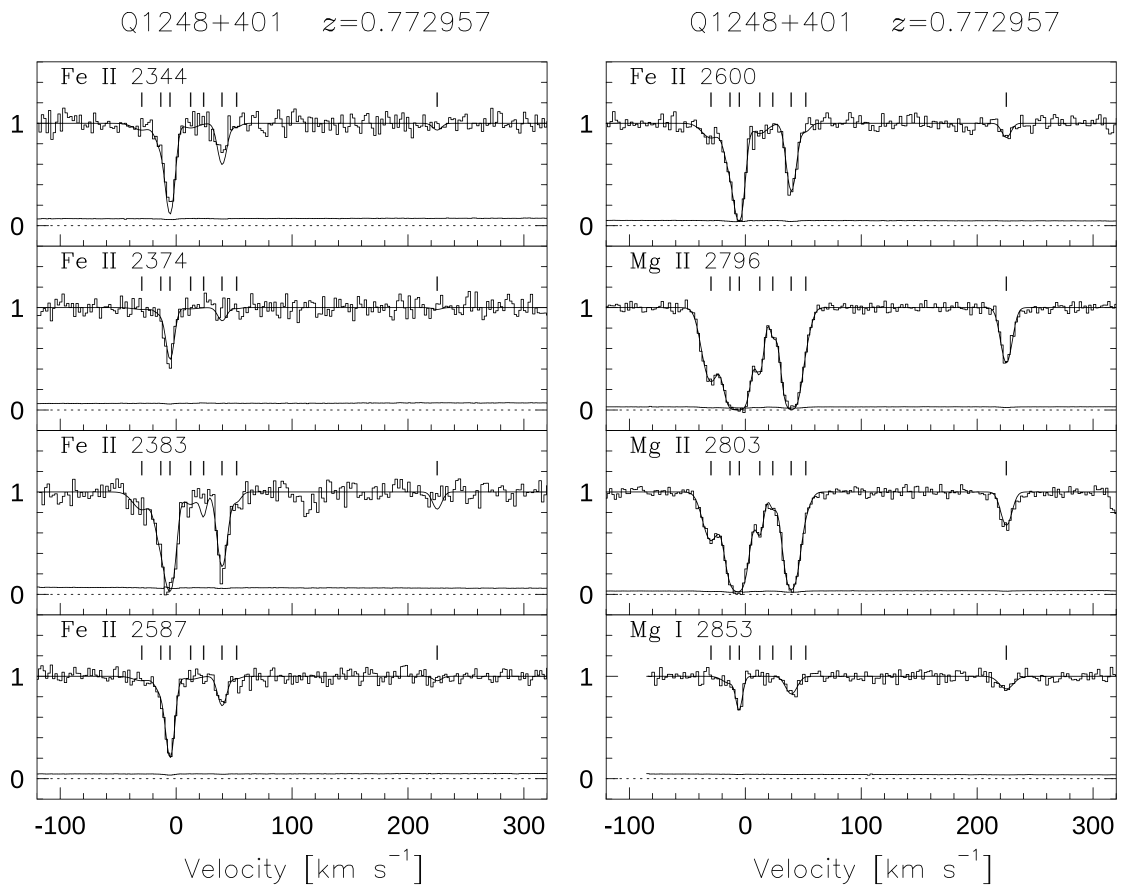

Fig. 3.43.— Q1248 + 401 at $z = 0.7730$: Absorption profiles and Voigt Profile fits.

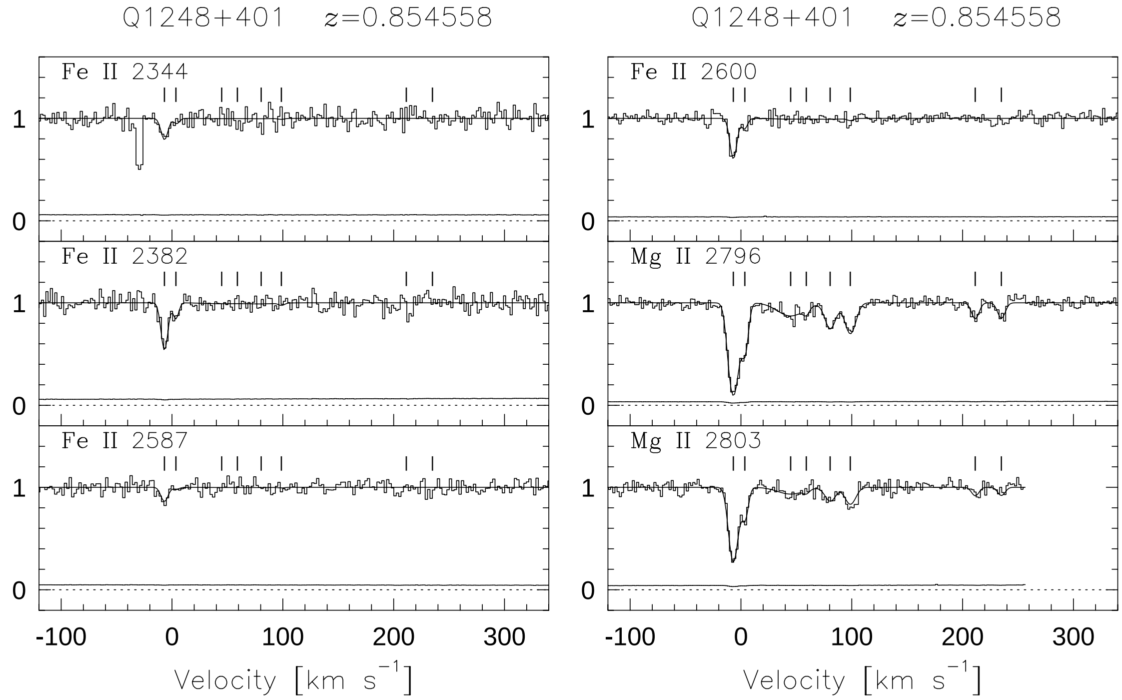

Fig. 3.44.— Q1248 + 401 at $z = 0.8546$: Absorption profiles and Voigt Profile fits.

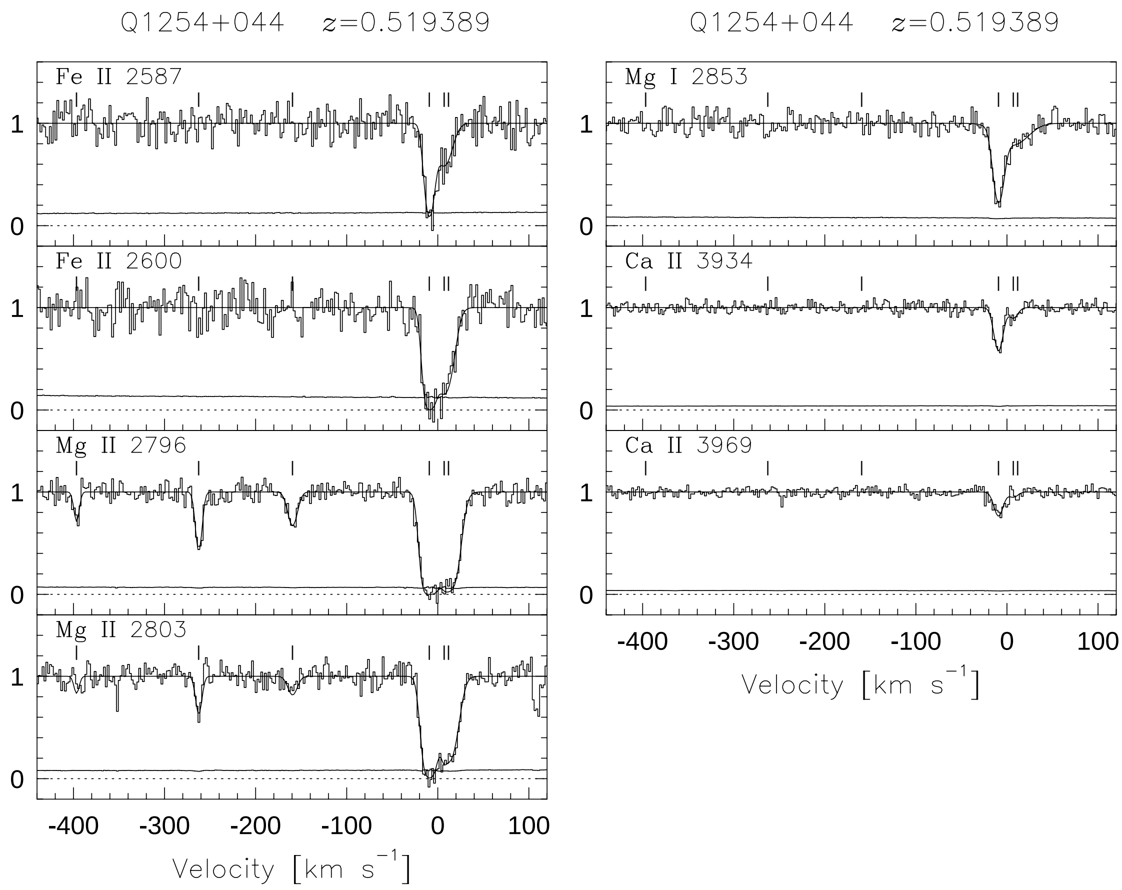

Fig. 3.45.— Q1254 + 044 at $z = 0.5194$: Absorption profiles and Voigt Profile fits.

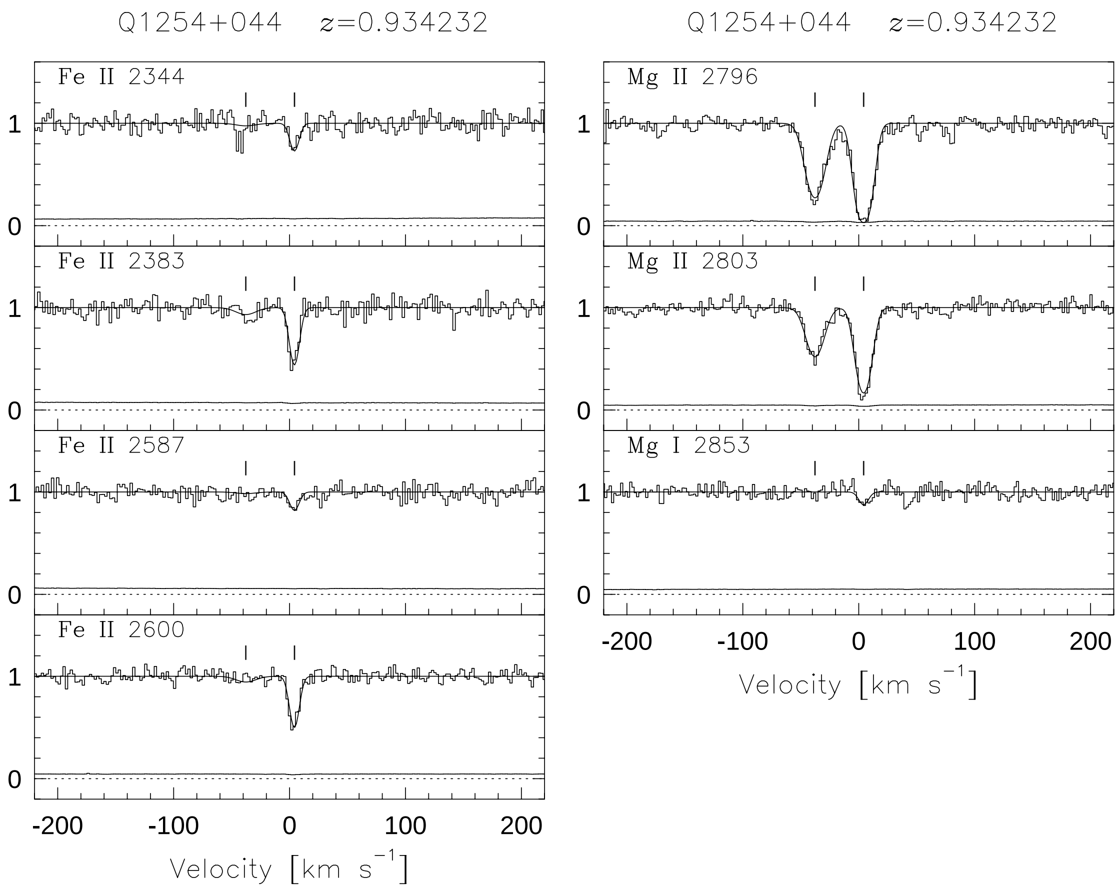

Fig. 3.46.— $Q1254+044$ at $z=0.9342$: Absorption profiles and Voigt Profile fits.

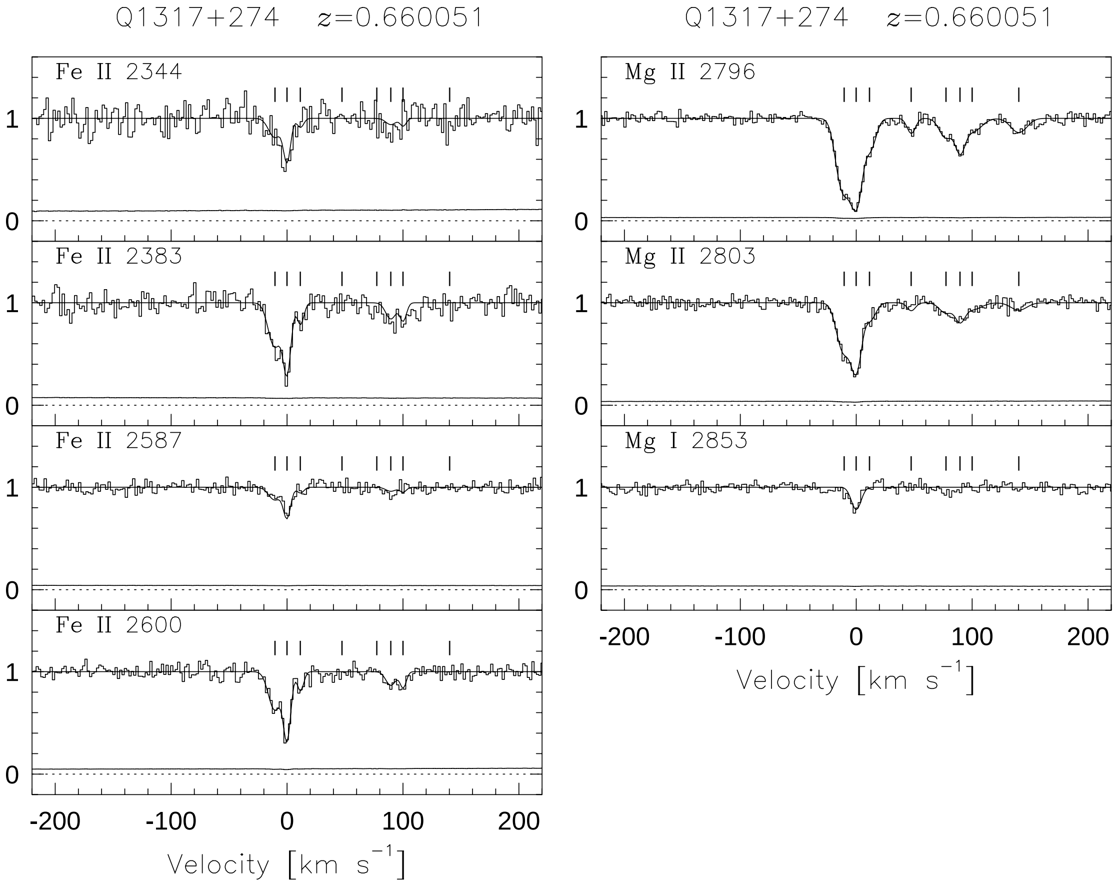

Fig. 3.47.— $Q1317+274$ at $z = 0.6600$: Absorption profiles and Voigt Profile fits.

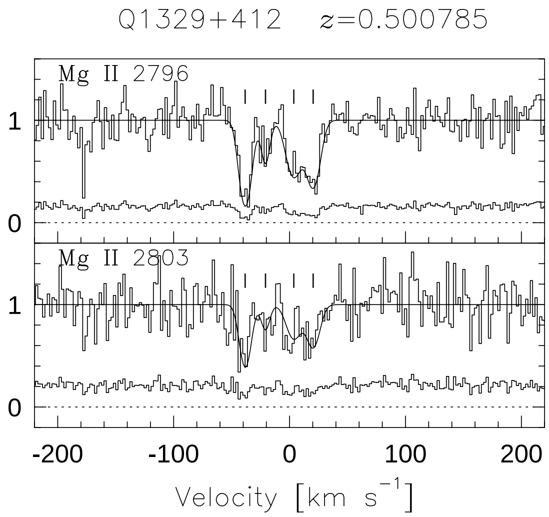

Fig. 3.48.— Q1329 + 412 at $z = 0.5008$: Absorption profiles and Voigt Profile fits.

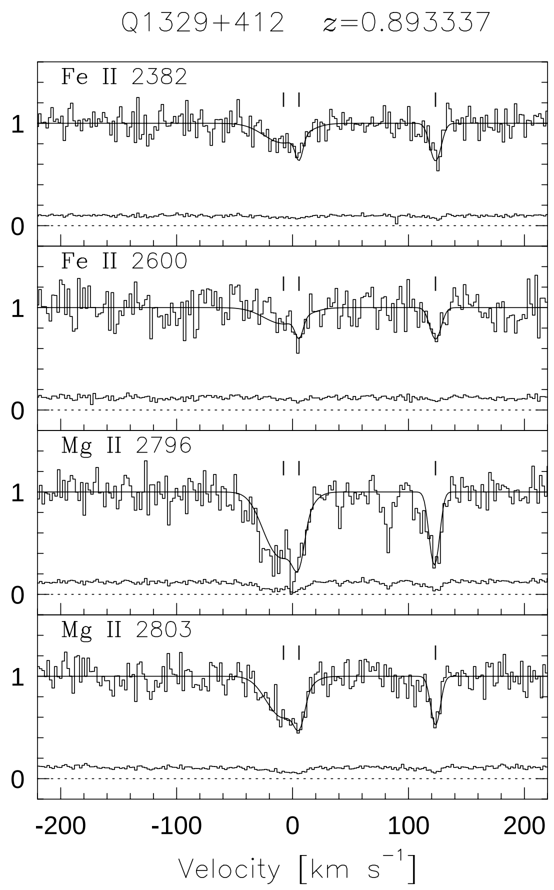

Fig. 3.49.— Q1329 + 412 at $z = 0.8934$: Absorption profiles and Voigt Profile fits.

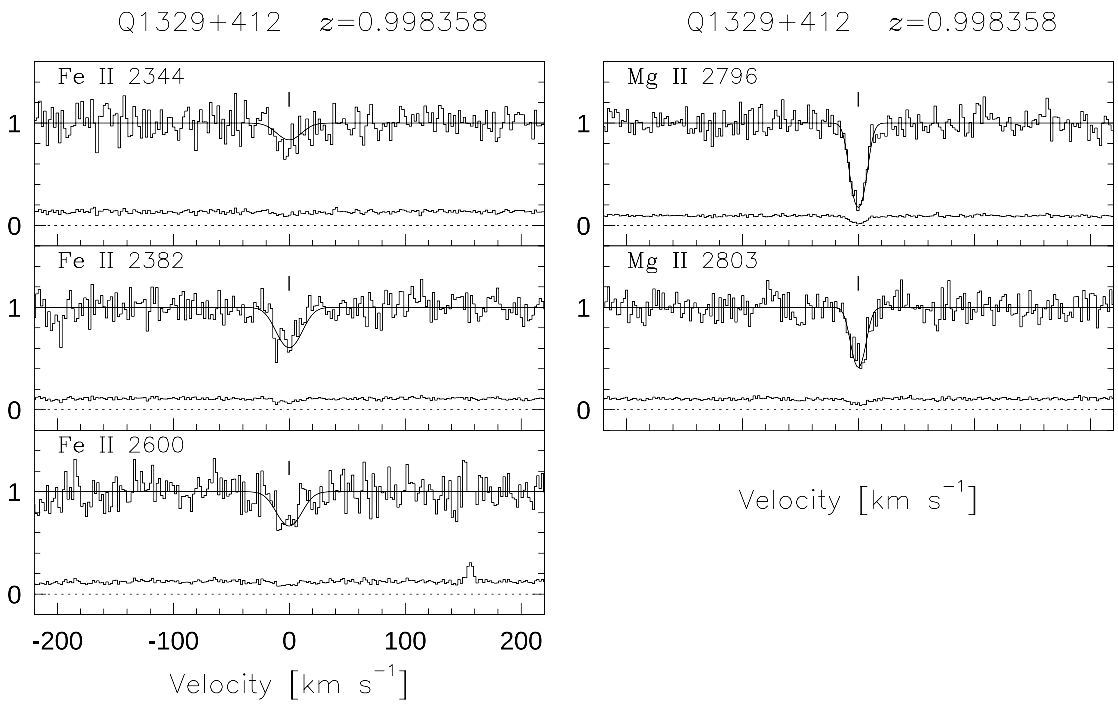

Fig. 3.50.— $Q1329 + 412$ at $z = 0.9984$: Absorption profiles and Voigt Profile fits.

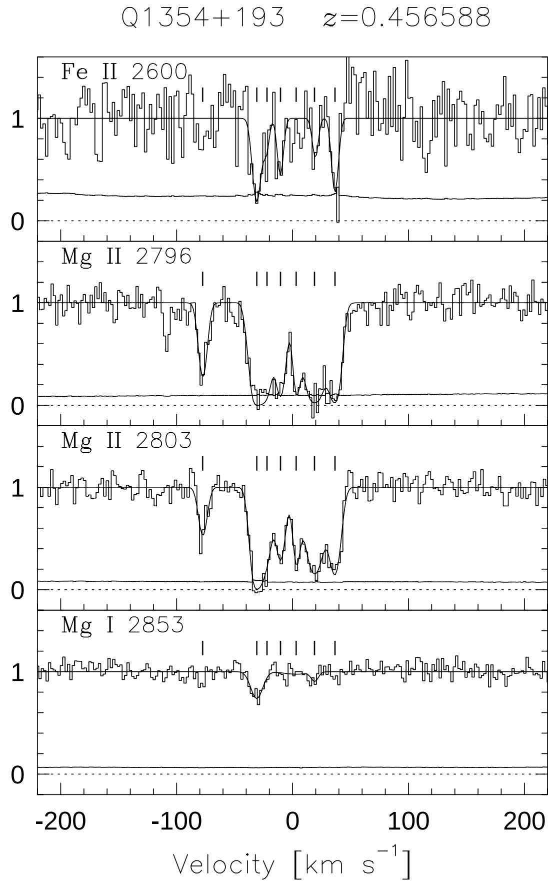

Fig. 3.51.— $Q1354+193$ at $z = 0.4566$: Absorption profiles and Voigt Profile fits.

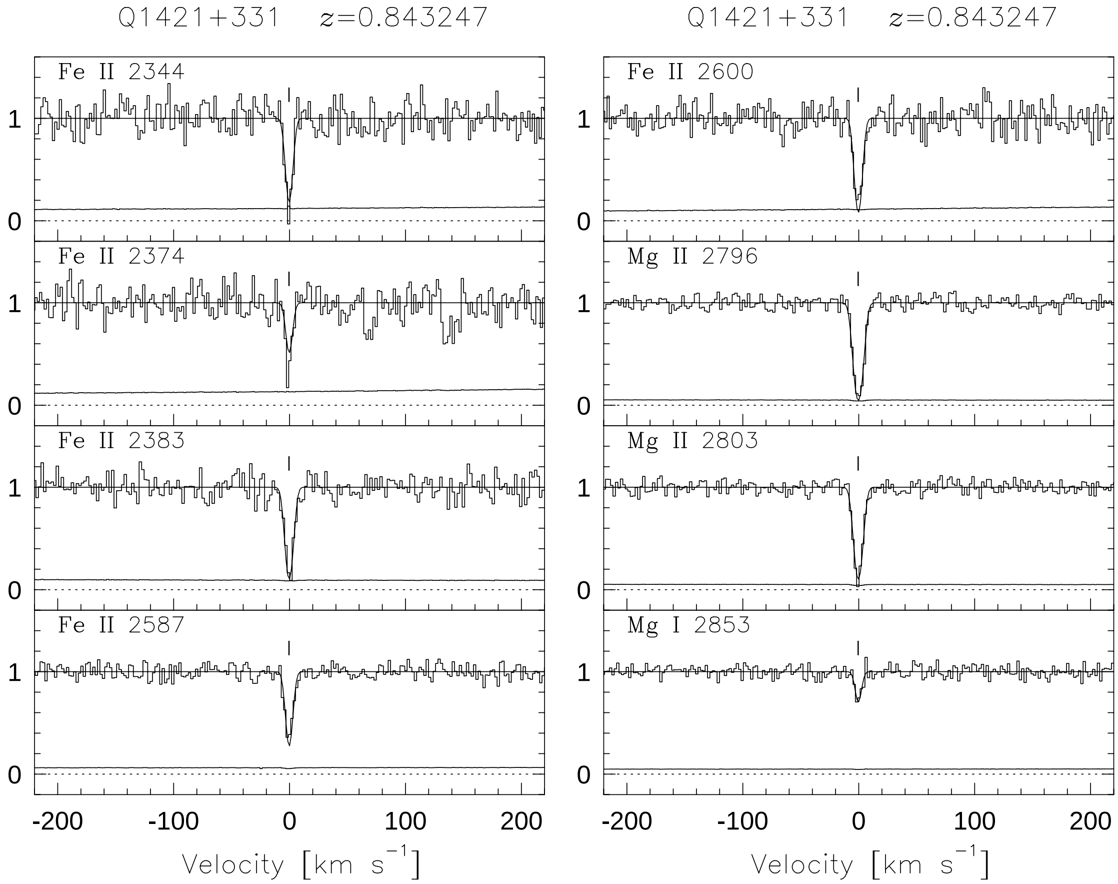

Fig. 3.52.— $Q1421+331$ at $z=0.8432$: Absorption profiles and Voigt Profile fits.

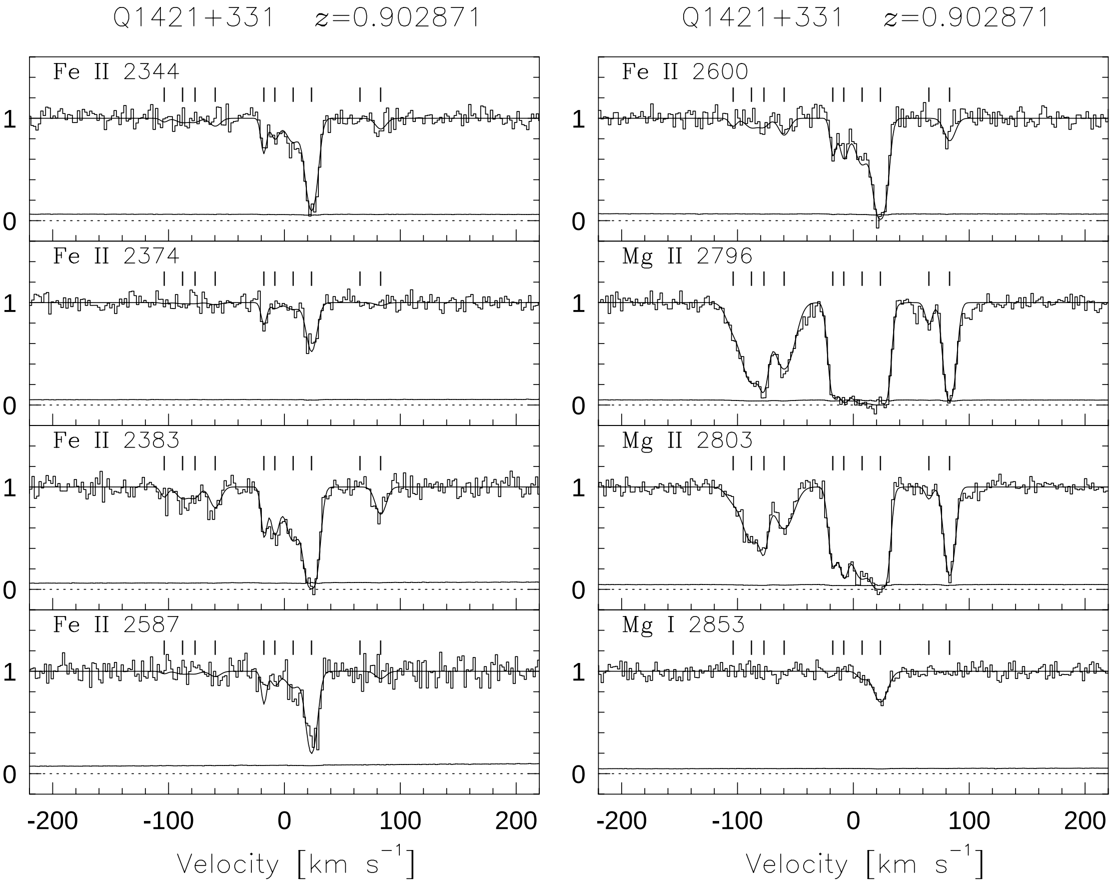

Fig. 3.53.— Q1421 + 331 at $z = 0.9029$: Absorption profiles and Voigt Profile fits.

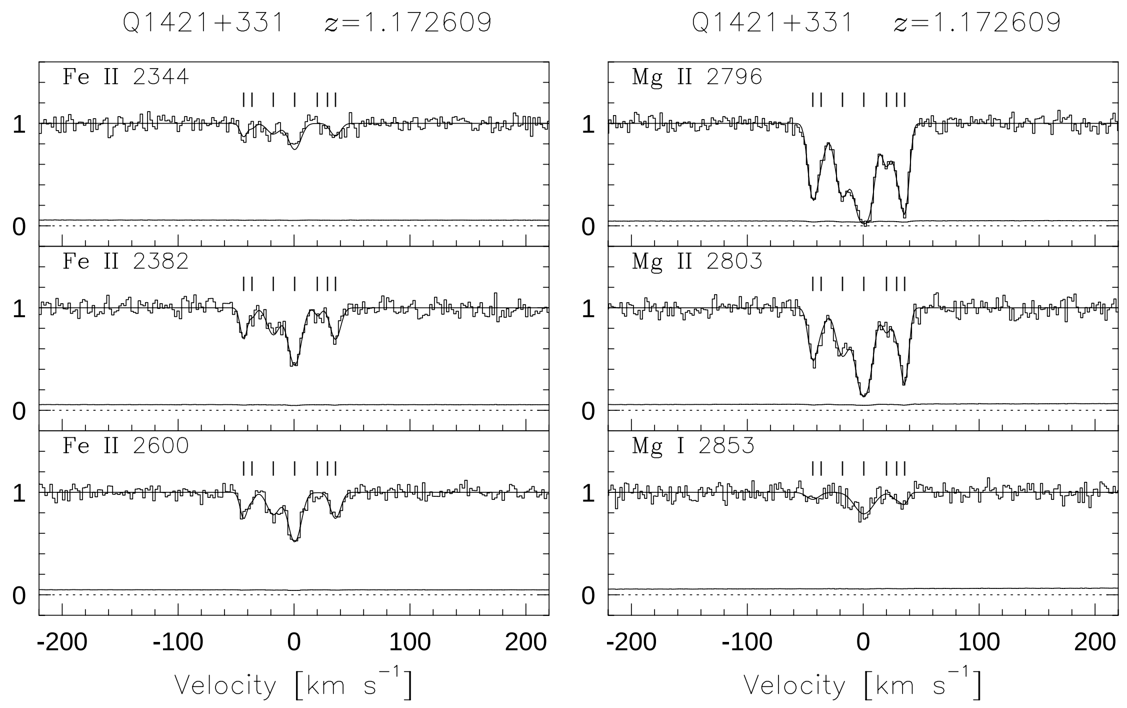

Fig. 3.54.— $Q1421+331$ at $z = 1.1726$: Absorption profiles and Voigt Profile fits.

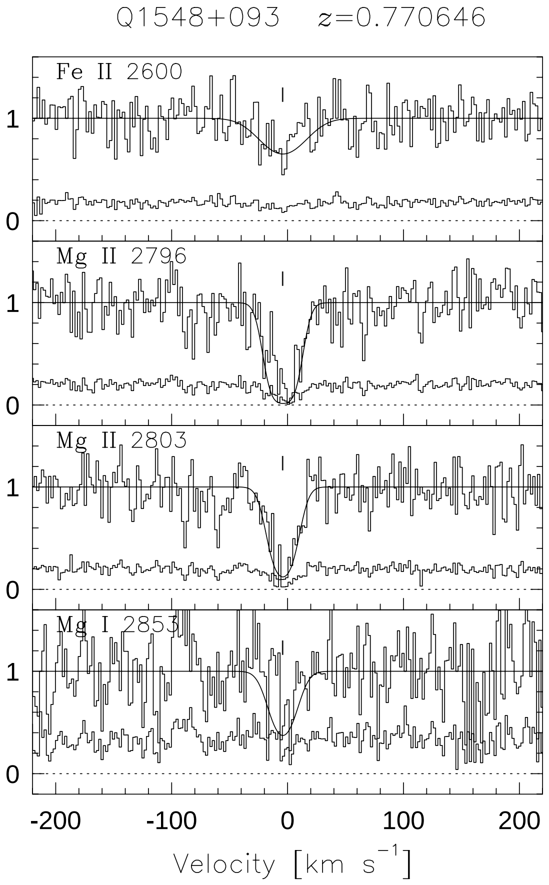

Fig. 3.55.— $Q1548+093$ at $z = 0.7706$: Absorption profiles and Voigt Profile fits.

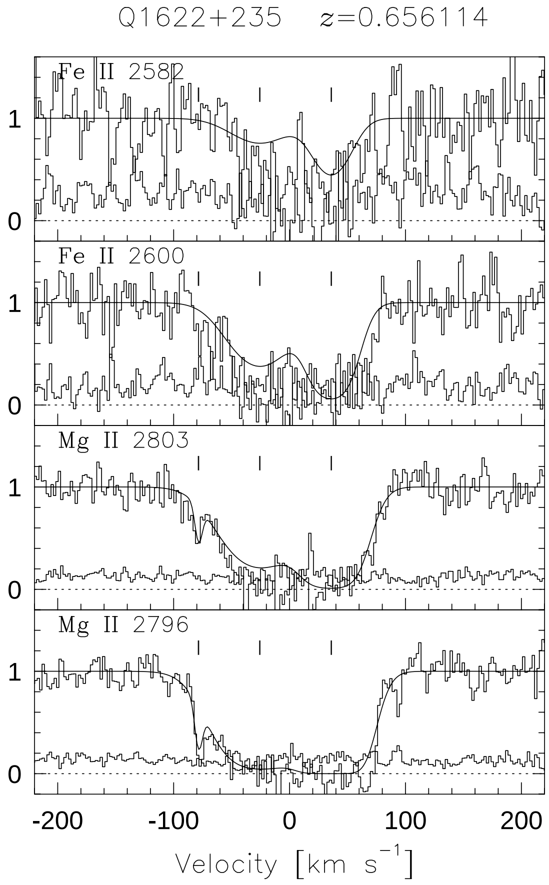

Fig. 3.56.— $Q1622 + 235$ at $z = 0.6561$: Absorption profiles and Voigt Profile fits.

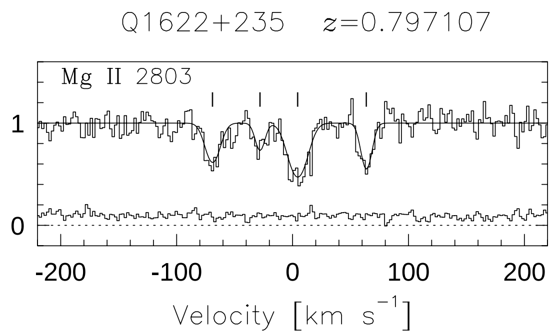

Fig. 3.57.— Q1622 + 235 at $z = 0.7971$: Absorption profiles and Voigt Profile fits.

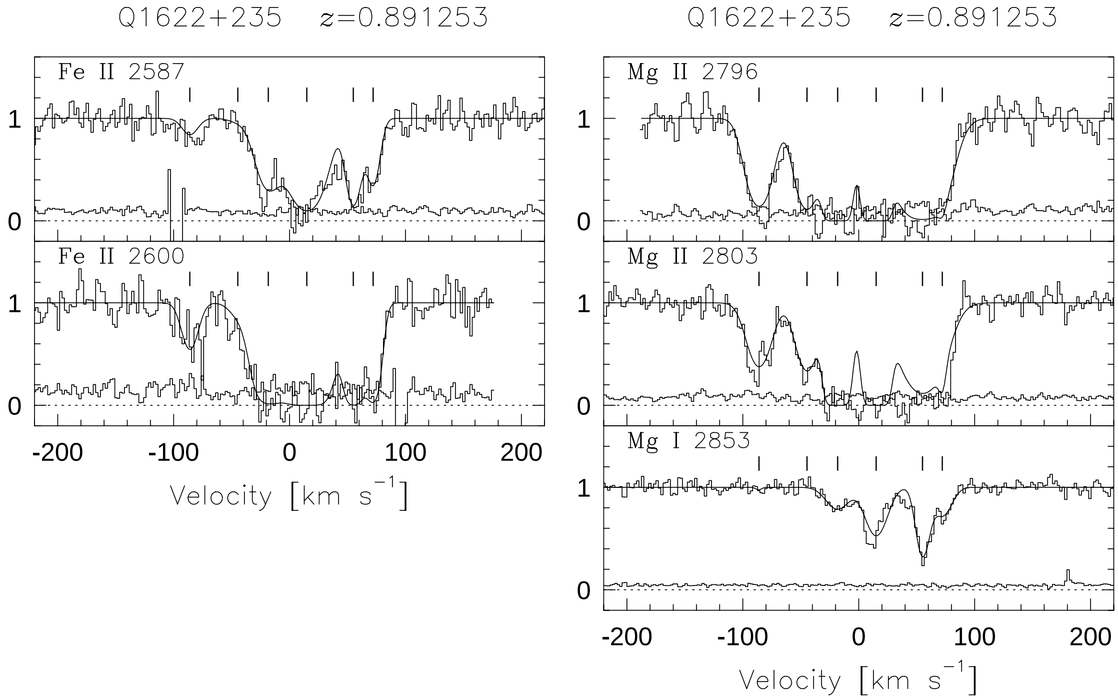

Fig. 3.58.— Q1622 + 235 at $z = 0.8913$: Absorption profiles and Voigt Profile fits.

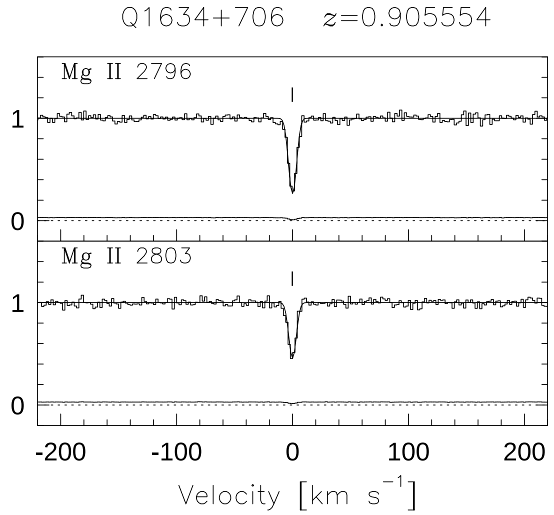

Fig. 3.59.— Q1634 + 706 at $z = 0.9056$: Absorption profiles and Voigt Profile fits.

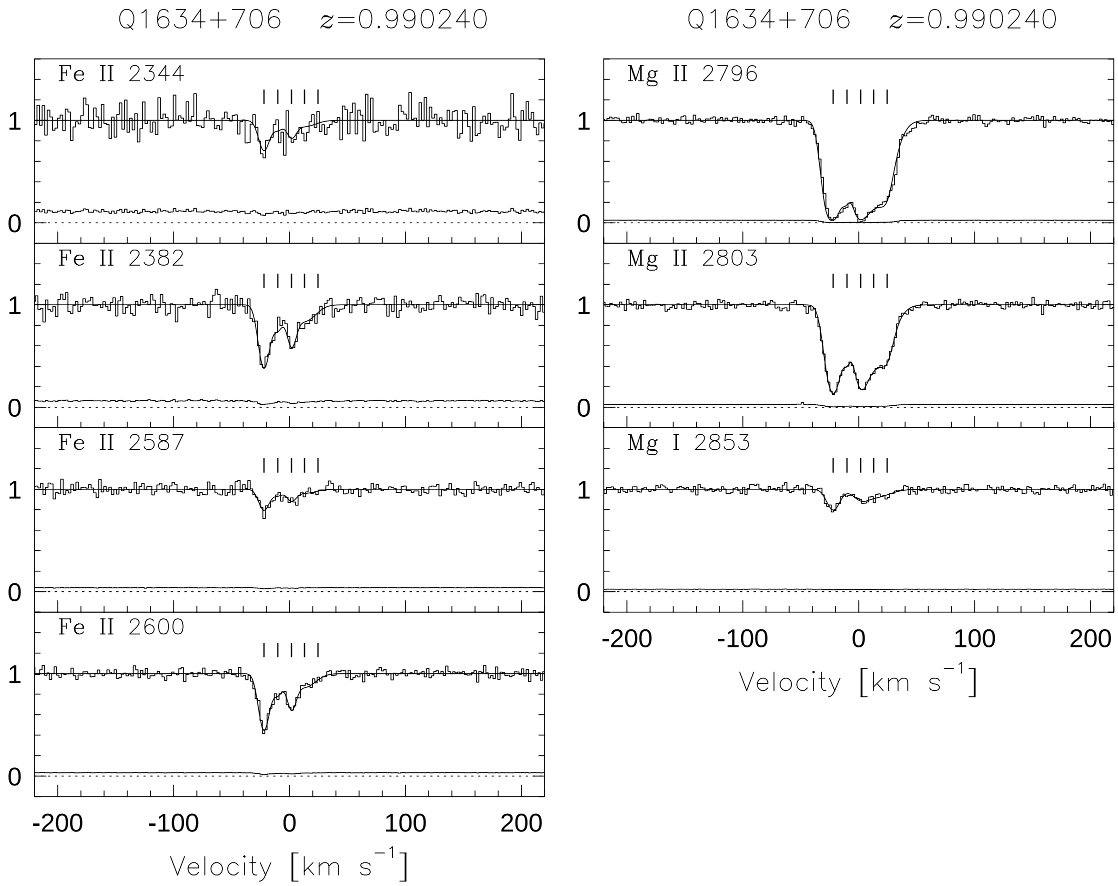

Fig. 3.60.— $Q1634 + 706$ at $z = 0.9902$: Absorption profiles and Voigt Profile fits.

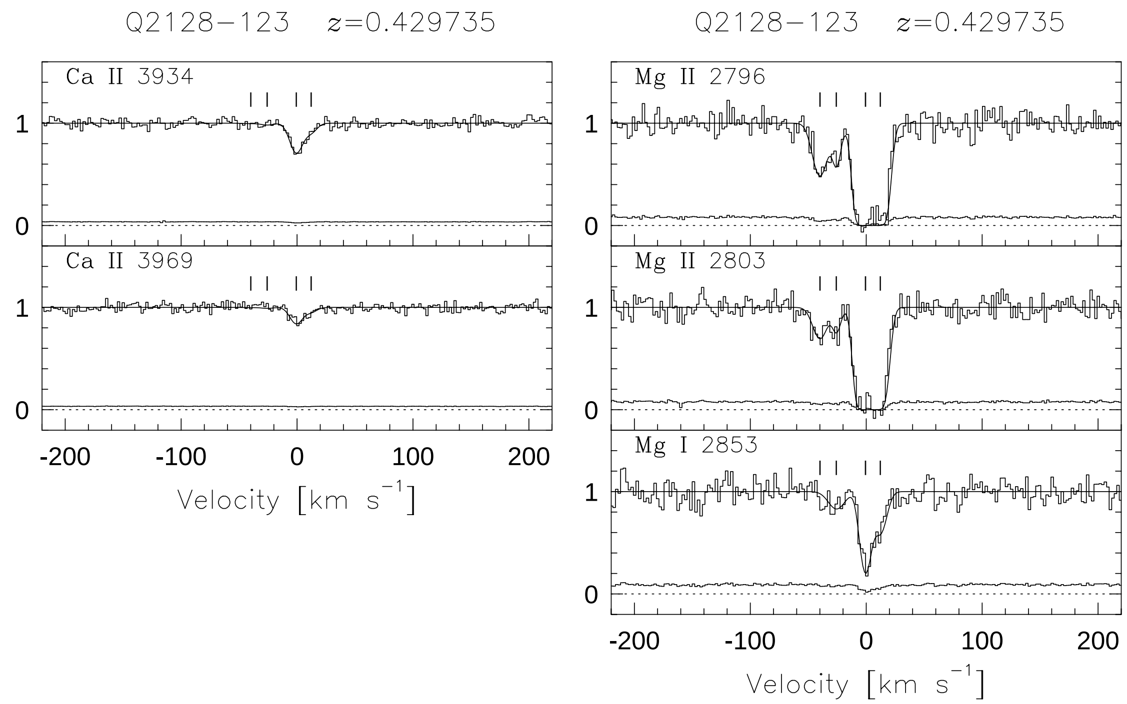

Fig. 3.61.— Q2128 − 123 at $z = 0.4297$: Absorption profiles and Voigt Profile fits.

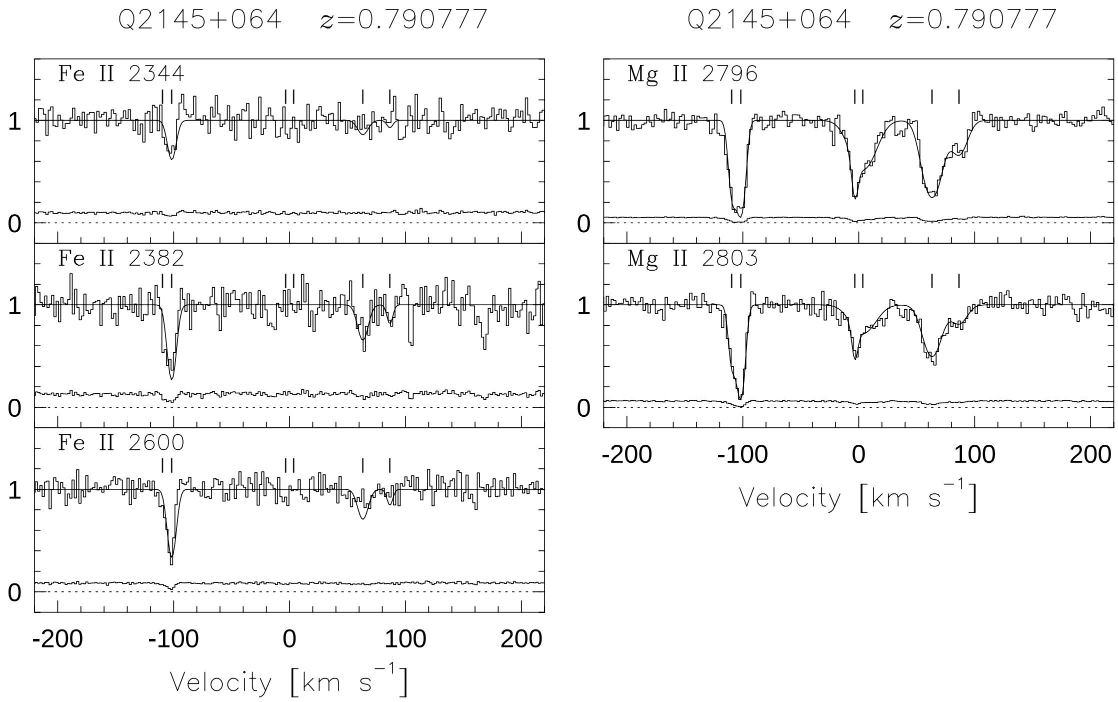

Fig. 3.62.— $Q2145+064$ at $z = 0.7908$: Absorption profiles and Voigt Profile fits.